21GRD02 BIOSPHERE

D1: Report on the characterisation, calibration and performance comparison of a mobile muon detector, a mobile neutron detector and a semiconductor based modified Timepix3 detector and the adaptation of a LIDAR system for vertical atmospheric profiling parameters (e.g., temperature, density, aerosol concentration) for use in determining SCR flux on the ground.

Organisation name of the lead participant for the deliverable: **PTB**

Due date of the deliverable: **Feb 2024** (M18)

Actual submission date of the deliverable: 30 September 2025

Confidentiality Status: PU - Public, fully open

Deliverable Cover Sheet

Funded by the European Union. Views and opinions expressed are however those of the author(s) only and do not necessarily reflect those of the European Union or EURAMET. Neither the European Union nor the granting authority can be held responsible for them.

European Partnership Co-funded by the European Union

METROLOGY PARTNERSHIP EURAMET

The project has received funding from the European Partnership on Metrology, co-financed from the European Union's Horizon Europe Research and Innovation Programme and by the Participating States.

Glossary

DPP	Digital pulse processing
EOLE	AErosol and Ozone Lidar systEm
HV	High voltage
ISO	International Organisation for Standardisation
LIDAR	Light detection and ranging
PCR	Primary cosmic rays
PMT	Photomultiplier tube
PSD	Pulse shape discrimination
SCR	Secondary cosmic rays
SiPM	Silicon photomultiplier
UV	Ultraviolet
USB	Universal serial bus
SEVAN	Space Environmental Viewing and Analysis Network

TABLE OF CONTENTS

1 Summary

To determine the dependence of SCR on PCR and atmospheric parameters, well-characterized particle and photon detectors for the SCR component and LIDARs for profiling atmospheric parameters are needed. This work presents the characterization, calibration, and performance tests of novel mobile particle detectors for measuring the muon and neutron components of SCR and the upgrade of two LIDAR systems for measuring aerosol mass, atmospheric density, and temperature profiles.

Section 2 addresses the characterization and calibration of PTB's mobile, position-sensitive, scintillator-based muon detector for measuring the muon component of the SCR. The sensitivity of the system to photons (X-rays and gamma rays) was investigated with reference X-ray fields according to ISO 4037 and ^{137}Cs and ^{60}Co gamma fields. The inherent background was investigated and determined at the PTB's underground laboratory, while the calibration with respect to ambient dose equivalent rate was performed at the PTB's environmental dosimetry site (ERADOS). Performance tests were also carried out at ERADOS, and the results were compared with PTB's reference instrument, which continuously measures charged component of SCR.

Section 3 presents the characterization of UJF CAS's novel mobile neutron detector based on boron scintillators, covering its sensitivity to neutron flux, energy dependency, and photon/neutron discrimination efficiency. The detector system was characterized and calibrated at the CMI in different reference fields for photons (^{137}Cs, ^{60}Co, X-rays 40-300 kVp) and neutrons (AmBe, Cf, thermal neutrons) to determine the neutron component of the SCR. Performance tests were carried out at the Lomnický Štít High Altitude Observatory (Slovakia) and the results were compared with those of the SEVAN detector, which continuously measures cosmic rays.

Section 4 presents the development, characterization, and calibration of ADVACAM's high-resolution particle telescope consisting of two Timepix3 pixel detectors arranged in close stacked architecture. The Timepix3 telescope tracker enables precise measurement and monitoring of the flux, composition, and direction of mixed radiation fields. The response of Timepix3 detectors with silicon and CdTe sensors to thermal and fast neutrons generated in well-defined reference radiation fields has been tested and evaluated in terms of radiation field visualization, flux, detection performance and neutron energy.

Section 5 addresses the upgrade of the NTUA EOLE and Raymetrics lidar system to meet BIOSPHERE requirements for measuring aerosol mass, atmospheric density, and temperature profiles. Hardware and software upgrades of the two LIDAR systems were summarized and discussed. In addition, the minimum and optimal measurement parameters, and the technical requirements for an optimal LIDAR system to determine the effects of atmospheric profiling parameters on the SCR flux to the ground were prospected.

Section 6 compares the capabilities of the BIOSPHERE SCR detectors with each other and with those of other neutron/muon detectors.

2 Metrological characterisation and calibration of a novel mobile detector for measuring the muon component of SCR

2.1 Introduction

Cosmic muons are an abundant and sustainable natural resource that can be used as a highly penetrating, non-destructive probe of the atmosphere, lithosphere, hydrosphere and cryosphere. Since their production rate depends on stratospheric temperature, while their absorption and decay depend on the density of the propagating medium, they can be used in several applications ranging from stratospheric monitoring and diagnostics to muon tomography of cyclones and lithographic structures, and for safeguarding of geological repositories (Zhang, 2020). Being charged particles, muons interact with the electrons of matter through electromagnetic forces. They lose energy through ionization and radiation loss. Common detection techniques include scintillation detectors, gas chambers (including cloud chambers), time-of-flight detectors, magnetic spectrometers, Cherenkov detectors and semiconductor detectors, with the choice depending on the specific requirements of the experiment or application (Grieder, 2001; Granja, 2018, Wissmann, 2005). For atmospheric, geological and climate-related applications, a portable detector is needed that can change its field of view on demand so that only selected parts of the atmosphere can be scanned. It should be pixelated so that density variations can be mapped, and it should be active so that it can continuously produce 2D maps or time dependent flux rate. While Cherenkov detectors and magnetic spectrometers are generally bulky and only used in large facilities such as IceCube or KM3Net, gas detectors and semiconductors can be used only for limited applications (e.g. gas-based detectors cannot be easily pixilated, while semiconductors - although pixilated - would be very expensive to realize with large active area). Scintillation detectors have many advantages compared to the alternatives above: they have high efficiency, have fast response times, are cost-effective and scalable.

PTB has developed a portable position-sensitive detector for measuring the muon component of the SCR. The detector consists of two detection units (see Fig. 1a) and operates in coincidence mode. The detector system is mounted on an aluminium frame which is rotatable (0° to 360°), tiltable (0° to 90°) and allows the distance between the two detector units to be changed (from 15 cm to 100 cm). Each detection unit consists of 20 scintillator paddles (Eljen technology, EJ-200) coupled via waveguides to silicon photomultipliers (SiPM), Fig. 1b.

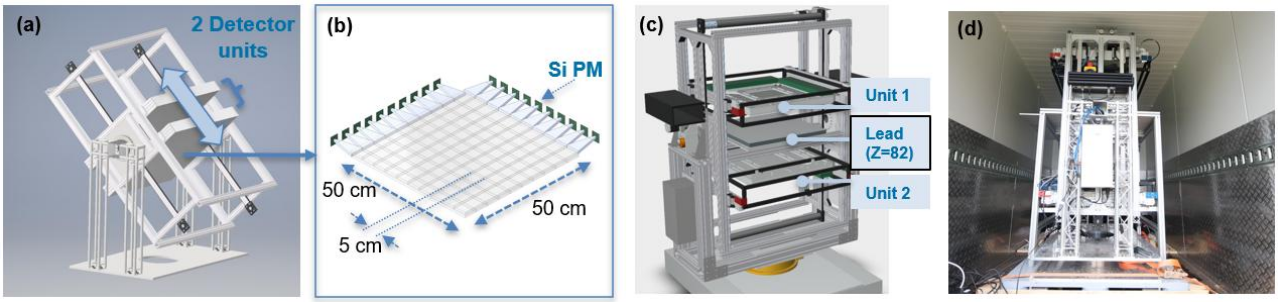

Figure 2.1 *Schematic drawings and a photo of PTB's position-sensitive muon detector DECOS2. (a) Schematic drawing of the aluminium frame with the two detector units. (b) Schematic drawing of one detector unit (top view). (c) Technical drawing of DECOS2 with 2.5 cm lead (Z=82) between the two detector units. (d) Photo of DECOS2 in a cooled trailer as it was used during the measurement campaigns in Athens and Brussels*.

In each detector unit, the scintillation paddles are arranged in two layers, each layer consisting of 10 paddles (Fig. 2.1b). The two layers are placed perpendicular to each other. This arrangement of scintillation paddles, in combination with coincidence detection, enables position-sensitive detection with a pixel size of 5 cm x 5 cm. The variable distance between the two detector units (without lead, from 15 cm to 100 cm) allows a field-of-view (FOV) of the detector between 0.79 sr/2π to 0.18 sr/2π.

2.2 Detector commissioning and functionality

All 40 detector segments (scintillator paddles) were functionally tested in a dedicated setup consisting of a Canberra preamplifier (Canberra 2006), a Canberra timing filter amplifier (Canberra 2111), and an Amptek Multi Channel Analyzer (MCA8000A), as well as home-built circuit boards for high voltage and operation of the SiPMT. Tests were made with a ^{90}Sr source which has a maximum beta energy of 2.28 MeV, close to the energy deposition by 4 GeV-muons ~2.36 MeV/cm (Groom, 2001). The ^{90}Sr source was placed on top of the scintillator with a 1 mm Al plate in between (Fig. 2.2(a)). A 1 mm thick Al plate placed between the scintillator and the source reduces the beta decay energy to 1.89 MeV. The source was positioned at three distances: in the central area of the scintillator bar to determine the threshold voltage of SiPM and for calibration purposes and, near and far to the conical light adapter to measure the signal loss along the scintillator bar. Each SiPM was operated with its nominal HV as quoted in the data sheet, including temperature compensation. For each detector segment the beta spectrum is measured (Fig. 2.2(b)). From these measurements, the number of UV photons at specific SiPM settings was determined. In addition, background rate vs. threshold settings were determined. As an example, Fig. 2.2(c) shows the number of UV photons generated by 2 MeV electrons; these tests were designed to test the functionality of each paddle.

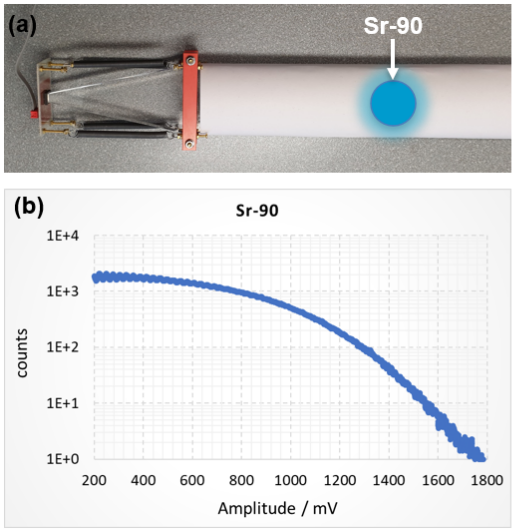

(c)

Number of photons measured and extrapolated for 2 MeVee deposited energy							
Detector 1				Detector 2			
Segment	photons / 2MeVee	SiPM #	HV (V)	Segment	photons / 2MeVee	SiPM #	HV (V)
Plane1				Plane1			
10	141	28	54.33	0	133*	44	54.20
11	131	25	54.08	1	132	45	54.96
12	135	23	53.97	2	129	43	53.99
13	129	22	54.29	3	136	46	53.96
14	130	34	53.76	4	124	42	54.32
15	128	40	54.30	5	132	47	53.96
16	129	39	54.00	6	133	41	54.35
17	130	27	53.83	7	136	6	53.78
18	153	21	54.20	8	141	29	53.90
19	113*	26	54.15	9	128	2	53.80
Plane 2				Plane 2			
0	106*	11	54.25	10	124	31	54.03
1	133	10	54.36	11	135	52	53.96
2	140	17	54.03	12	122	51	54.02
3	128	12	54.27	13	137	16	53.97
4	133	19	54.13	14	135	50	53.9
5	129	15	53.98	15	136	55	53.99
6	131	13	54.31	16	147	49	53.92
7	134	32	53.76	17	134	54	54.06
8	122	33	53.80	18	138	53	54.04
9	125	14	54.08	19	114*	48	53.94

Figure 2.2 ***(a)*** *Experimental setup used to test the performance of each scintillator paddle.* ***(b)*** *Pulse height distribution of ^{90}Sr beta radiation on a scintillator bar.* ***(c)*** *Estimated number of photons per 2 MeV "electron equivalent" in Polyvinyltoluene scintillation bars*.

The light generated by the radiation in the scintillators is passed through Plexiglas conical adapter to the SiPMs (Hamamatsu S13360-6050CS) located on each scintillator. Each SIPMs has a dedicated circuitry board for the voltage supply and temperature corrections (Fig. 2.3). The signal from the silicon photomultiplier is passed on to the respective home-build amplifier board. There the signal is amplified by three amplifier stages and then evaluated by a comparator. The comparison voltage of the comparator is controlled with a digital potentiometer so that the threshold at which a signal is further processed can be adjusted.

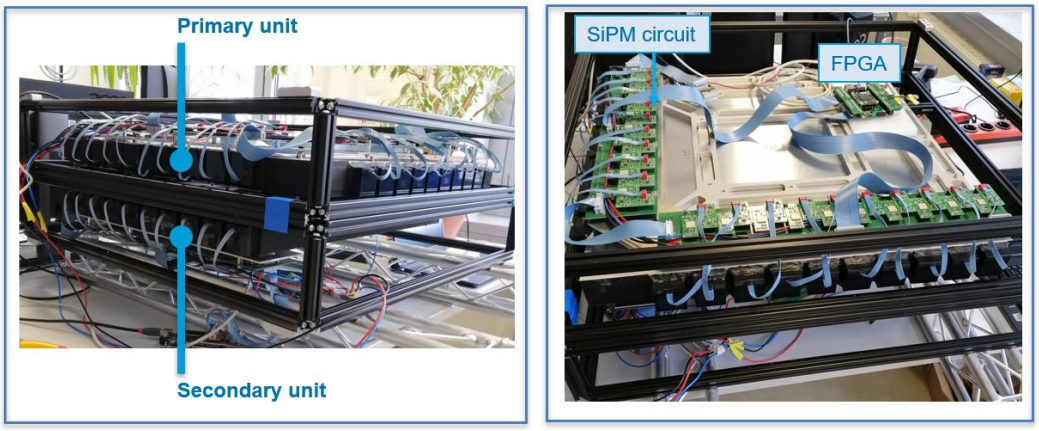

Figure 2.3 *Detection units of DECOS2*.

All signals from the 20 amplifier boards of each detector unit are then further processed by a Field Programmable Gate Array (FPGA) of Spartan-6 family (Spartan-6 XC6SLX100-2), see Fig. 2.3. In the first step, an attempt is made to form 2-point (double) coincidences from the signals measured in both units (both units have each 20 channels). The timer (or coincidence window) can be set between 10 ns and 80 ns in 10 ns steps. If no coincidence signal is detected, the signal is rejected. Once a coincidence signal has been detected, the primary detector unit, which is usually at the top, tries to form 4-coincidences from the 2-coincidences measured at both units. The clocks of the two FPGAs are synchronized via data connection and the double coincidences of the secondary detector unit are transmitted to the primary detector unit. With the synchronized clocks, the time stamps of the two most recent 2-coincidences are simply compared to form the 4-coincidences. The timer for a valid 4-point coincidence is usually +/- 20 ns but can be changed to +/-40 ns. The 4-coincidences and 2-coincidences are sent from the primary detector unit to the measuring computer via USB. This happens as a 19-digit hexadecimal code in which the FPGA clock timestamp and the channels are encoded, as well as the information about which data it is. They are then saved on the measuring computer with the time stamp of receipt.

Figure 2.4 shows the 2D distributions of the DECOS2 4-coincidences (quadruple coincidences) for a 4-day measurement at the PTB environmental dosimetry site (ERADOS). These distributions represent maps of charged part of the SCR (muons + electrons) and were measured with a separation between units of 15 cm and without lead. The slight difference in intensity distributions between the two detector units is due to the fact that few events (about 3%) hitting the first detector are distributed across multiple pixels in the secondary units (3 and 4 hits).

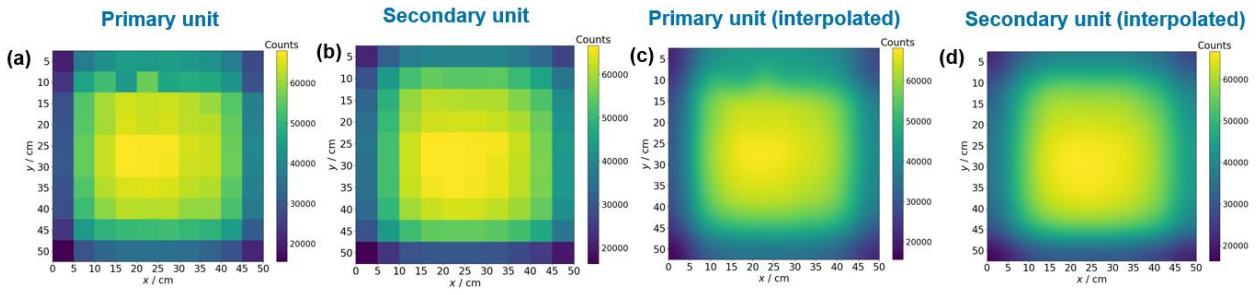

Figure 2.4 *2D distribution of the quadruple coincidences measured by the DECOS2: (a) Distribution measured in the primary and* ***(b)*** *in the secondary detection unit. Bicubic interpolation of the* ***(c)*** *primary and* ***(d)*** *secondary unit signals*.

The sensitivity of the detector units to x-ray and gamma radiation fields was tested with reference x-ray fields according to ISO 4037 (N-series, 150 kV and 300 kV, with dose rates up to 3 mSv/h) and ^{137}Cs and ^{60}Co

gamma fields (up to 1 µSv/h at a distance of about 1 cm from the detector unit), see Fig. 2.5(a). No signal above the background could be measured with X-ray fields and ^{137}Cs (Fig. 2.5 (b,c)). However, the 2D distribution of ^{60}Co source could be measured (see Fig. 2.5(d)). This indicates that the Compton electrons produced by the high-energy gamma fields (>662 keV) have enough energy to generate UV photons on both scintillator layers of the primary (secondary) detector units. Therefore, DECOS2 is sensitive to photons with energies higher than 662 keV with respect to double coincidences. This sensitivity can be eliminated by using a 2.5 cm thick lead between the two detector units, or by increasing the separation between the detection units to more than 50 cm.

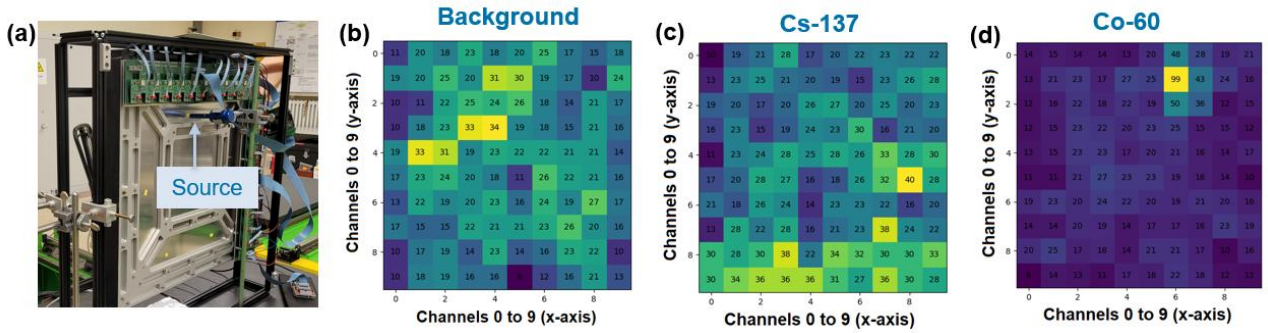

Figure 2.5 *Example of a 2D distribution of 2-fold coincidences in one of the DECOS2 units (integration time: 60 s).* ***(a)*** *Experimental setup with one of the DECOS2 units and a ^{60}Co source placed 1 cm above the detector.* ***(b)*** *2D distribution of the background.* ***(c)*** *2D distribution of the measured counts using a ^{137}Cs source.* ***(d)*** *2D distribution of measured counts using the ^{60}Co source. Counts are indicated in the pixels*.

2.3 Measurements at the underground laboratory

The characterization of DECOS2 with the reference gamma fields (^{60}Co) and the determination of the inherent background were carried out in PTB's underground laboratory. Due to the depth of 430 m below ground, the cosmic ray muon intensity in this facility is reduced by more than 3 orders of magnitude compared to ground level. In addition, the low specific activity of the pure rock salt and a moderate activity concentration of radon in air (< 10 Bqm^{-3}), as well as the use of well selected materials with a specific activities less than 2 Bq/kg, result in an extremely low ambient dose equivalent rate $\dot{H}^*(10)_{bg,UDO}$ =(1.5 ± 0.2) nSv/h (Röttger, 2018).

The irradiation setup is shown in Fig. 2.6(a). The reference point is marked by the reference lasers, which are an integral part of the calibration facility. Measurements were performed at three reference positions of DECOS2 relative to the irradiation source (see Table 2.1). Figure 2.6 (b) shows the 2D distribution of the ^{60}Co reference field measured with the primary detection unit at 0.7 m over 20 minutes. The size of the field is about 25 cm, which agrees well with the expected value of 24 cm defined by the lead collimator with an opening angle of 20°. The 2D signal integrated over 1 minute is shown in Fig. 2.6(c). With 1 minute integration time the relative uncertainty is about 4%. This value is improved considerably (to below 2%) when increasing the integration time to 10 minutes, which is the standard operation time.

Table 2.1 Reference ambient dose equivalent rate $\dot{H}^*(10)$ at different reference positions of DECOS2.

Reference distance / m	$\dot{H}^*(10)$ / (nSv/h)
0.7	993.5 ± 15.0
2	121.7 ± 1.9
3	54.1 ± 0.9

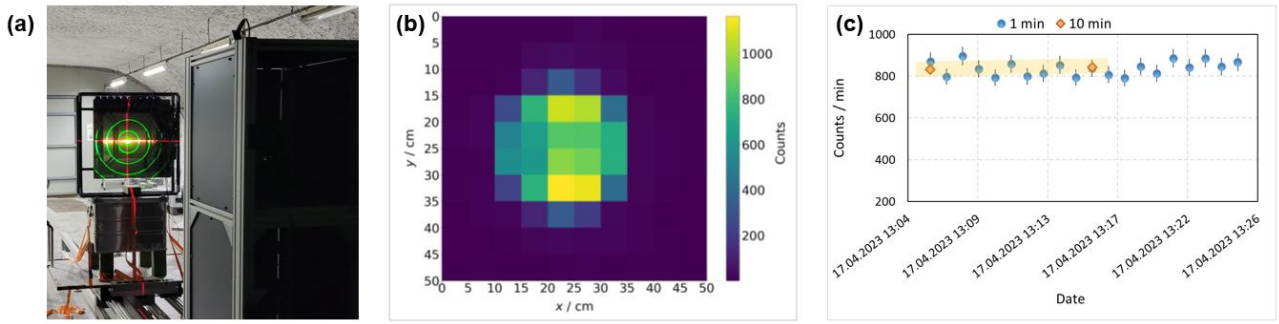

Figure 2.6 ***(a)*** *Irradiation facility at UDO II used to test the response of DECOS2 detection units to Co-60 reference fields.* ***(b)*** *Image of the ^{60}Co beam at a 0.7 m reference distance.* ***(c)*** *Time integrated signal measured with Co-60 reference field at 0.7 m from the source*.

Figure 2.7(a) shows the 2D distribution of the inherent background in the primary unit (twofold coincidences) measured over 30 min, while 2.7(b) shows the time integrated signal measured over 3 days. This would correspond to measurement of inherent background with quadruple coincidences when both units have zero separation between them (i.e., measurement over 2π steradian). The measured inherent background is 13±4 counts/10 min, about 1380 times smaller than the value measured at the ground level, as expected. For FOV corresponding to 1 m separation between the detection units no quadruple coincidence was measured, indicating that the flux of muons is less than 1 muons/(cm^2 ·3 days·2π) and would correspond to a flux reduction of more than 5000x. This agrees well with the expected flux reduction at 1 m distance 1380/0.18=7666, with 0.18 sr being the FOV of the detector at 1 m.

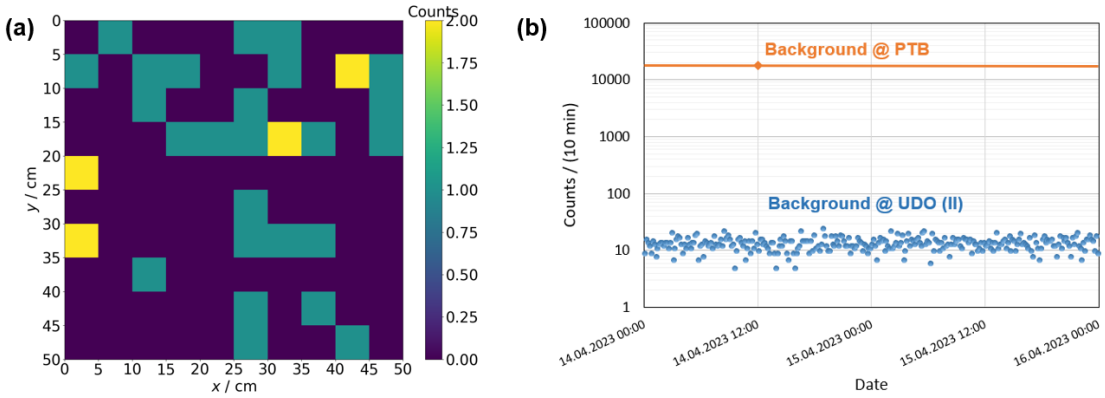

Figure 2.7 *Inherent background of DECOS2.* ***(a)*** *2D distribution of inherent background measured over 30 minutes.* ***(b)*** *Time dependence of inherent background measured over 3 days*.

2.4 Calibration and performance of muon detector

DECOS2 was cross calibrated at PTBs ERADOS, which contains a number of detectors that continuously measure secondary cosmic rays, terrestrial gamma radiation and radon as well as atmospheric parameters such as temperature, air pressure, humidity and precipitation (Dombrowski, 2012). The reference standard used for the cross-calibration was the DEtector system for COSmic radiation (DECOS1) which allows coincidence measurements based on two large area plastic scintillator panels (EJ-200 Polyvinyltoluene, 80 cm x 80 cm x 2.5 cm) arranged one above the other and read out by two photomultipliers. The coincidence rates of DECOS1 were calibrated in terms of $H^*(10)$ due to SCR (including both muons and electrons) using a tissue-equivalent proportional counter (TEPC) reference instrument, which is surrounded by a multiwire

proportional counter, in order to distinguish charged particles from photons (Wiesmmann, 2005). Both detectors (DECOS2 and DECOS1) were run simultaneously, side-by-side, pointing vertical, same azimuth.

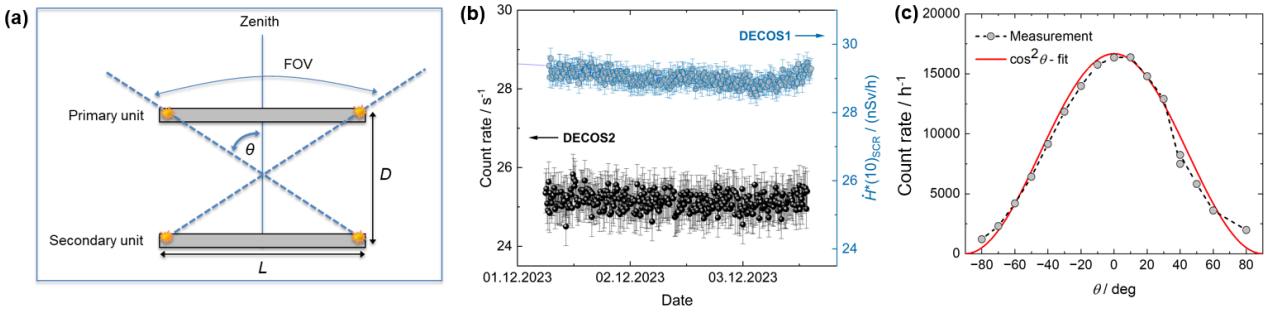

Figure 2.8 ***(a)*** *Schematic view of detector geometry.* ***(b)*** *Simultaneous measurements of SCR at ERADOS with DECOS1 and DECOS2. Here, DECOS2 was operated with D=15 cm and without lead between the two detection units.* ***(c)*** *$\cos^2\theta$-dependence of muon intensity measured with DECOS2 at ERADOS.*

To convert count rates from DECOS2 to $\dot{H}^*(10)$ using the reference instrument DECOS1, the conversion coefficient k_{DECOS2} need to be determined. This conversion coefficient can be calculated as

$$k_{\mathrm{DECOS2}} = \frac{\dot{H}^*(10)_{\mathrm{ref}}}{J_{\mathrm{DECOS2}}}$$

with $\dot{H}^*(10)_{\mathrm{ref}}$ being the ambient dose equivalent rate measured with the reference instrument DECOS1 and J_{DECOS2} the acceptance-averaged differential intensity measured with DECOS2:

$$J_{\mathrm{DECOS2}} = \frac{R_{\mathrm{DECOS2}}}{G_{\mathrm{DECOS2}}} .$$

Here, R_{DECOS2} denotes the DECOS2 4-fold coincidence rate (in counts · s^{-1}), and G_{DECOS2} is the geometrical factor for two-element telescopes with rectangular symmetry [see J.D. Sullivan, *Geometrical factor and directional response of single and multi-element particle telescopes*, Nucl. Instrum. Methods **95** (1971) 5–11]. The resulting angle-averaged differential intensity, J_{DECOS2}, has units of $cm^{-2}\cdot s^{-1}\cdot sr^{-1}$, while G_{DECOS2} has units of $cm^2\cdot sr$.

With a separation D=15 cm between the two detector units of DECOS2 during calibration, the following values were obtained: R_{DECOS2}=(25.15±0.03) s^{-1}, G_{DECOS2}=(4552±313) $cm^2\cdot sr$, and J_{DECOS2}=(5.5±0.5)×10^{-3} $cm^{-2}\cdot s^{-1}\cdot sr^{-1}$. The conversion coefficient k_{DECOS2} for $\dot{H}^*(10)_{\mathrm{ref}}$ =(29.0±4.9) nSv/h is

k_{DECOS2}=(5250 ± 980) (nSv/h)·$cm^2\cdot sr\cdot s$=(1.46 ± 0.27) nSv·$cm^2\cdot sr$.

The omnidirectional muon flux at the ground level (an altitude of approx. 75 m) is $J_2 \approx \pi\cdot J_{\mathrm{DECOS2}} \approx 1$ $cm^{-2}min^{-1}$. This value agrees well with the values published in the literature [M. Tanabashi et al. (Particle Data Group), Phys. Rev. D 98, 030001 (2018); P. K. F. Grieder, Cosmic rays at Earth, Elsevier (2001)].

Figure 2.9 shows the muon flux measured by DECOS2 relative to that measured by the reference instrument DECOS1 and atmospheric pressure. From the figure it is evident that the time dependence of DECOS2 data compares well with the data measured by DECOS1 and is anti-correlated with the pressure due to absorption of muons by the air column, indicating that DECOS2 can resolve well atmospheric effects in the muon flux. Although the experimental standard deviation of the muon flux rate in DECOS2 is larger than in DECOS1 (about 40 %), it is still sufficient to resolve atmospheric pressure effects in the flux rate.

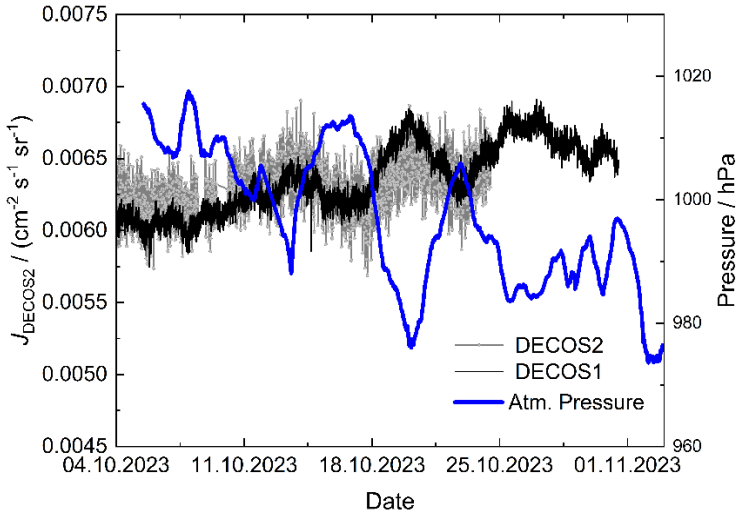

Figure 2.9 *Temporal evolution of DECOS1 and DECOS2 data relative to atmospheric pressure. During these measurements DECOS2 was operated with D=100 cm and 2.5 cm lead between the detection units. To highlight time dependent trends, DECOS1 data (which were measured without lead) have been scaled accordingly*.

2.5 Summary

PTB has developed a portable position-sensitive detector for measuring the muon component of the SCR. The detector system (DECOS2) is mounted on an aluminum frame which can be rotated (0° to 360°) and tilted (0° to 90°) and allows the distance between the two detector units to be changed (from 15 cm to 100 cm). The arrangement of the scintillation paddles in combination with coincidence detection enables position-sensitive detection with a pixel size of 5 cm x 5 cm. The variable distance between the two detector units enables a field of view (FOV) of the detector between 0.79 sr/2π and 0.18 sr/2π. Its sensitivity to photons (X-rays and gamma rays) was investigated with reference x-ray fields according to ISO 4037 and Cs-137 and Co-60 gamma fields. Only photons with energies greater than 662 keV can generate double coincidence signals, however no measurable quadruple coincidences in both detector units. Gamma photon suppression is further enhanced by using a 2.5 cm thick lead layer between the two detection units. The inherent background was determined in PTB's underground laboratory, while the calibration with respect to $\dot{H}^*(10)$ was performed at the PTB's environmental dosimetry site. The time dependence of quadruple coincidences indicates that the detector can resolve well atmospheric effects in the muon flux.

3 Characterisation, calibration and performance of neutron detector for use in determining SCR flux on the ground

3.1 Introduction

The novel detector of Nuclear Physics Institute of the Czech Academy of Sciences (UJF CAS) for measuring the neutron component of SCR is based on two liquid scintillators EJ-309B2.5 with pulse shape discrimination capabilities – 2x2“ EJ-309 with ^{10}B content of 2,5%, PMT 9214B 51 mm and 5x5“ EJ-309 with ^{10}B content of 2,5%, PMT 9390B 130 mm, coupled with CAEN digitizer DT5730S with firmware DPP PSD (Figure 3.1).

This neutron detector can measure neutrons in a wide range of energies (from thermal up to several tens of MeV). Compared to other neutron detectors it is small and portable and is able to separate photons and neutrons based on pulse shape discrimination (Sommer, 2022).

Figure 3.1 *Neutron detector – large scintillator 5x5" (left), small scintillator 2x2" (center), and box with all components (right).*

The pulses from PMTs can be digitized and saved to the computer in raw version, or they can be digitally processed by the CAEN digitizer. The raw pulses were used for the optimization of the PSD (pulse shape discrimination) algorithm, while energy calibration and discrimination of thermal neutrons were done with already processed pulses. The processing of individual pulses consists of several steps - calculation of the baseline; removing the background; calculating the trigger position using Constant Fraction Discrimination (CFD) method; calculation of the whole pulse area (long gate), corresponding to the deposited energy; calculation of the part area of the pulse (short gate); calculation of Charge Comparison Method (CCM), proportion of short and long gate.

3.2 Characterization of the mobile neutron detector

The neutron detector was characterized in several reference photon (^{137}Cs, ^{60}Co, X-ray 40-300 kVp) and neutron (AmBe, Cf, thermal neutrons) fields at Czech Metrology Institute (CMI) (Figure 3.2).

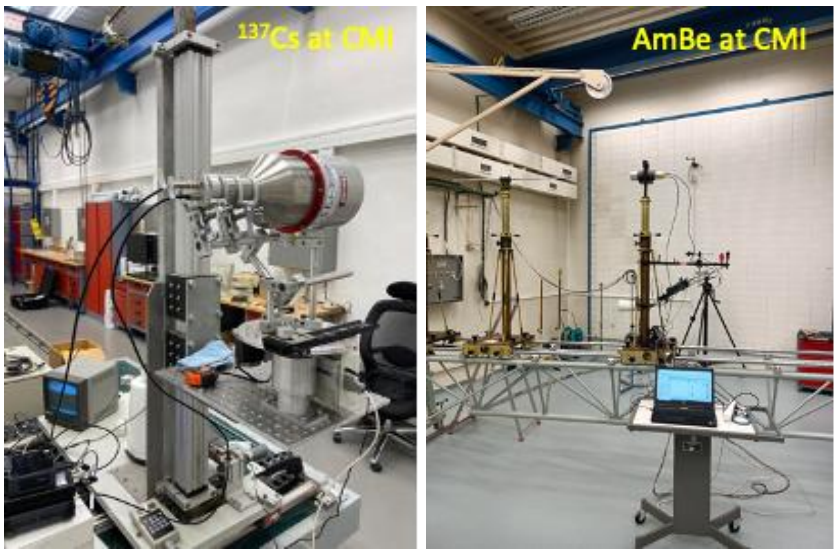

Figure 3.2 *Characterization of the detectors at CMI. Left - angular dependence in photon field; right - energy dependence in high-energy neutron fields.*

3.2.1.1 Setting the optimal parameters (short gate and long gate) and adjusting the sampling frequency

For the optimization of the pulse shape discrimination capabilities, both scintillators were irradiated with AmBe source at CMI. Used shielding helped to remove 60 keV photons originating from ^{241}Am in the source that largely contributed to the number of registered events.

The steps of a procedure for optimization of photon/neutron discrimination are shown in Figure 3.3 (for scintillator 5 x 5"). 2D histograms of all measured particles from the deposited energy (long gate) characteristics and the charge comparison method (CCM) value were created, then individual slices of deposited energy (each slice corresponds to 200 a.u. of deposited energy) were fitted by Gaussian mixture module (GMM). Parameters of fits were used to calculate a Figure of Merit (FOM) which indicates how well the individual Gaussian curves can be separated. The higher the value, the better the discrimination between photons and neutrons. The separation line was calculated from the individual separation values using linear interpolation and extrapolation.

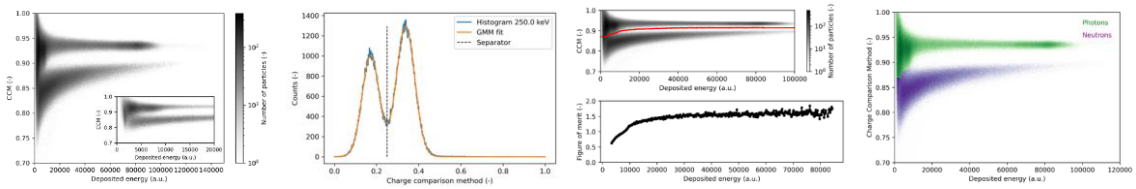

Figure 3.3 *a) 2D histogram; b) Histogram and GMM fit for particles with deposited energy 200-300 keVee; c) Separation line between neutron and photon components and FOM as a function of deposited energy; d) Final distribution of the neutron and photon components*.

The previous steps were repeated several times for different lengths of short gate (6 to 82 ns, 4 ns step). The best discrimination of the neutron and photon components was achieved at a short gate length of 26 ns for the 2x2" scintillator and 82 ns for the 5x5" scintillator.

3.2.1.2 Calibration of photon and neutron spectra

The photon spectra calibration was done using the Compton edges of discrete gamma sources (^{22}Na, ^{137}Cs, ^{60}Co, shielded AmBe after discrimination of photon component). The location of Compton edges was identified as the minima of differentials of smoothed spectra. The calibration curve uses the following equation:

$$y = a*log(bx+1)+cx \quad (1)$$

where *a, b, c* are fitting parameters.

To determine the deposited energy from fast neutrons, the following equation was used:

$$y = ax - (b*(1-exp(-cx)) \quad (2)$$

where *a, b, c* are parameters found in [Enqvist et al., 2013], *x* is proton recoil energy and *y* is electron equivalent energy.

3.2.1.3 Discrimination of thermal neutrons

The identification of thermal neutrons is based on the reaction with ^{10}B, which results in an alpha particle and a lithium ion with large LET (linear energy transfer). Due to the energy quenching, the final light output is significantly lower than it would be if the same energy was deposited by a low LET particle.

To define the thermal neutron regions, the detector was irradiated at CMI at a thermal neutron prism that generates a thermal neutron field by thermalizing fast neutrons from AmBe sources.

The identification of thermal neutrons was done via thresholding of 2D histograms. Two channels were used for thermal neutron discrimination. The first channel records the alpha particles produced in the reaction of a thermal neutron on boron. Due to energy quenching, alpha particles with high LET appear to be detected at energies of 60-100 keV and over a wide range of CCMs (from 0.6-0.9), i.e., over both the photon and neutron spectra. The second channel is due to photon radiation with an energy of 478 keV, which is emitted with a high probability of 94% in the reaction of thermal neutrons with boron. If the gamma radiation is deposited in the detector volume, the pulse superpositions with the pulse from the alpha particle to produce a channel with a CCM smaller than the photon spectrum but not low enough to fit into the neutron spectrum. The resulting channels defining the thermal neutrons for both smaller and bigger detectors are shown in Figure 3.4.

There is an overlap between individual regions, therefore, they are contaminated by other types of different radiation.

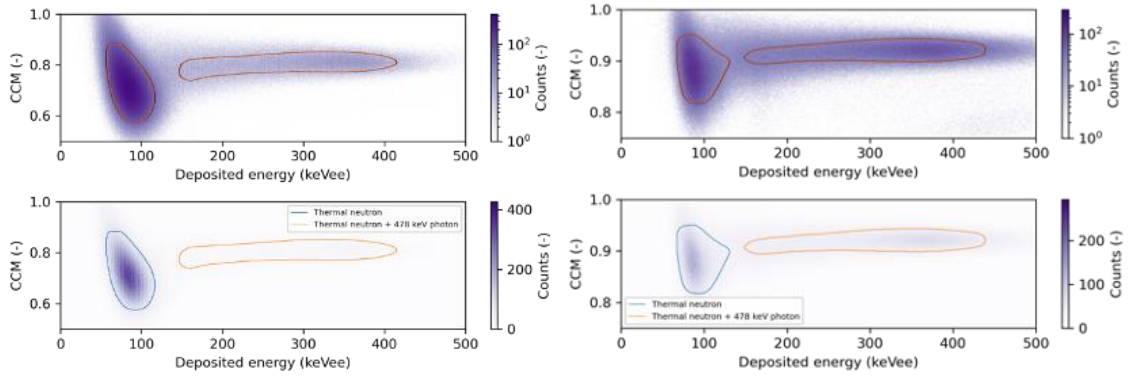

Figure 3.4 *Discrimination of thermal neutrons for 2x2" scintillator (left) and 5x5" scintillator (right). The top row shows 2D histograms in a logarithmic scale and the bottom row in a linear scale*.

3.2.1.4 Energy resolution and energy dependence

The energy resolution of scintillators was determined by minimization of the Gaussian convoluted Monte Carlo spectrum of ^{60}Co and ^{137}Cs and measurements of ^{60}Co and ^{137}Cs. The parameters of Gaussian distribution applied to the ideal MC calculated spectrum were a function of deposited energy. The FWHM of Gaussian distribution followed the equation:

$$FWHM = \sqrt{a^2 + \frac{b^2}{E} + \frac{c^2}{E^2}} \qquad (3)$$

where the parameters *a*, *b*, *c* are fitting parameters and *E* is the deposited energy by photons. The neutron energy resolution was calculated by combining Eq. 2 and Eq. 3. The overall energy resolution for the 5x5" scintillator can be seen in Fig. 3.5.

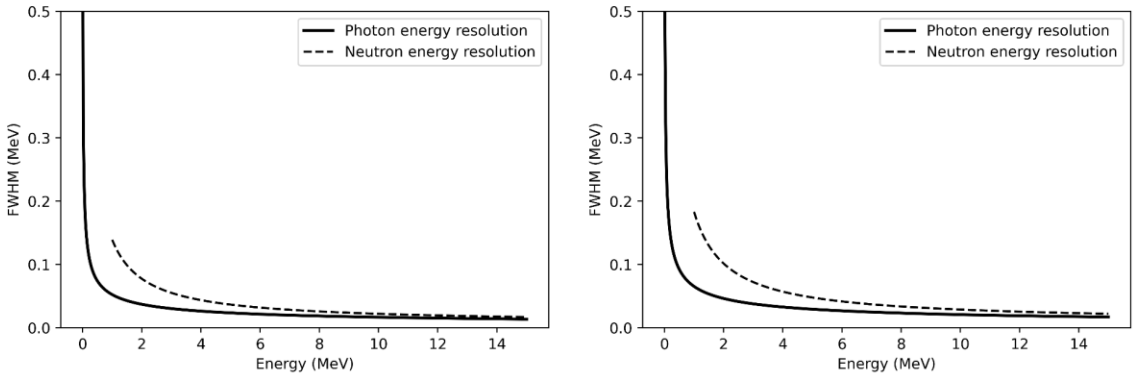

Figure 3.5 *The photon and neutron energy resolution of 2x2" (left) and 5x5" (right) scintillators plotted as a function of energy.*

The detector energy dependence was measured in X-ray beams and photon fields of ^{137}Cs and ^{60}Co radionuclides. In Fig. 6 the comparison of the measured and Monte Carlo simulated energy dependence is plotted for the 2x2" scintillator.

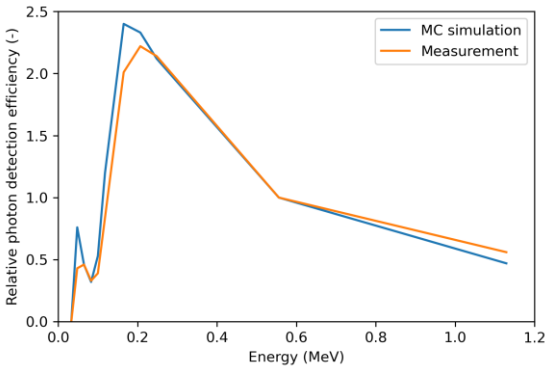

Figure 3.6 *The comparison of measured and Monte Carlo simulated energy dependence of the 2x2" scintillation detector.*

The detection efficiency was derived from Monte Carlo simulations of ^{252}Cf and AmBe neutron sources. The detection efficiencies of fast neutrons were calculated based on the response of the detectors to recoil protons and detection efficiencies of thermal neutrons were derived from the probabilities of reactions on ^{10}B. The detection efficiencies are tabulated in Table 3.1.

Table 3.1: Tabulated values of neutron relative detection efficiency and count rate per unit fluence of 2x2" and 5x5" scintillators derived by Monte Carlo calculations.

	Detection efficiency (%) **2x2" | 5x5"**	**K ((counts/s) / (cm^{-2}s^{-1}))** **2x2" | 5x5"**
^{252}Cf - fast neutrons	**25.3 | 37.5 (1)**	**5.1 | 47.5**

AmBe - fast neutrons	**27.9 | 44.8 (1)**	**5.7 | 56.7**
Prism - thermal neutrons	**78.5 | 84.8 (2)**	**20.4 | 143.0**

(1) For neutrons with E > 1 MeV via recoiled protons;
(2) For thermal neutrons via neutron absorption on ^{10}B.

3.3 The Monte Carlo simulations

Monte Carlo (MC) models of both neutron scintillation detectors (Figure 3.7) were developed in the general-purpose radiation transport code MCNP in version 6.2 according to technical drawings and datasheets. Validation of the models was performed in reference photon beams at CMI by the comparison of measured and simulated energy dependence, such as depicted in Figure 3.7. Sensitivity and angular dependence were calculated as well.

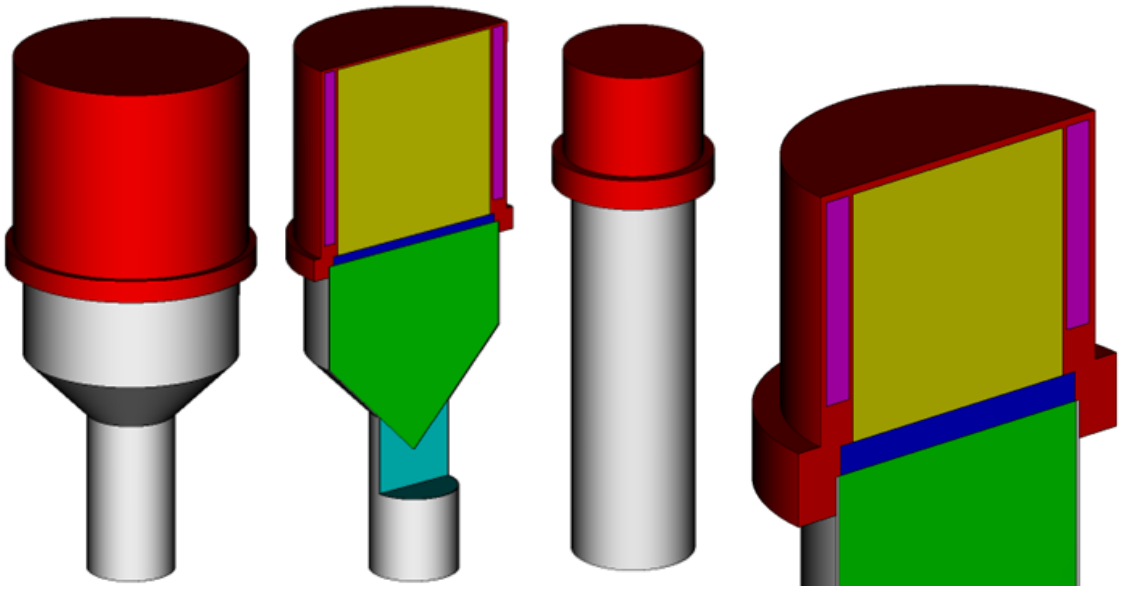

Figure 3.7 *Visualization of MC model of the large scintillation detector (left two) and the small scintillation detector (right two). Colours distinguish materials*.

The scored quantity was the energy deposition in the liquid scintillator separately for each type of charged particles. In photon fields, this was achieved by the F8-type tally. In neutron fields, the task was more complex because of interaction of thermal neutrons with ^{10}B in the scintillator resulting in emission of several secondary particles, which needed to be treated independently because of different effects on the detector response. Therefore, a PTRAC (particle track) file was generated and later offline processed, allowing to separate energy deposition of a) photons emitted during B-10 disintegration, b) all other photons, c) alpha and Li-7 ions emitted during B-10 disintegration, d) recoiled protons and ions detected in coincidence with “c)”, and e) all other recoiled protons and ions. Availability of such information allowed offline analysis and modifications leading to better understanding the detection processes for the analysis of measured data, especially the separation of counts from different particle types, thermal neutron detection with and without coincident detection of a 478 keV photon, and to the composition of the final detector spectra.

Figure 3.8 presents examples of such decomposed detector spectra for AmBe and thermal neutron fields. The spectra do not include the effect of energy resolution and light collection efficiency.

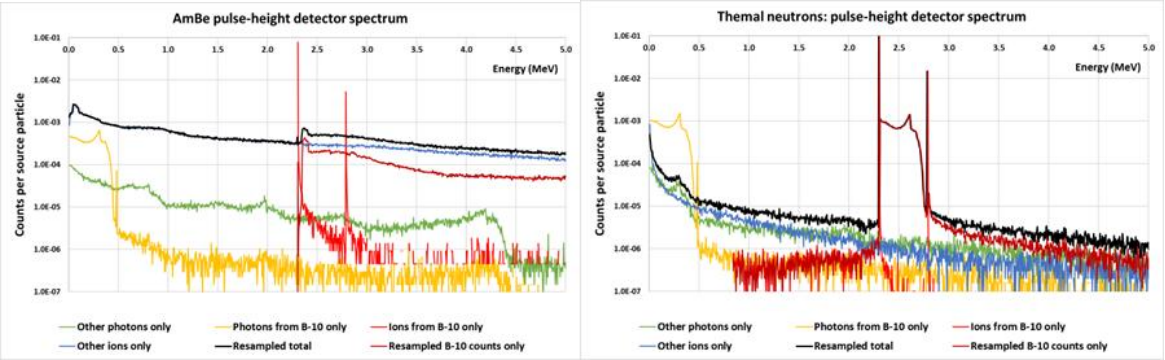

Figure 3.8 *Example of detector spectra generated by AmBe neutron source (left) and thermal neutron field (right) decomposed into contributions of different groups of particles taking into account coincident detection of particles initiated by the same original neutron*.

3.4 Performance of neutron detector

In summer 2022, the neutron detector was placed at the high-mountain observatory Lomnický Štít, Slovakia. An example of time series data is shown in Figure 3.9. Brief enhancements in the photon channel are caused by radon progenies during the precipitation. Due to the overlapping of the regions, the similar enhancement can be seen in neutron channels (especially the thermal neutrons). Nevertheless, fast neutrons with energies higher than 2 MeV are not correlated with radon progenies enhancements since neutrons with higher energies are more reliably discriminated by the PSD algorithm.

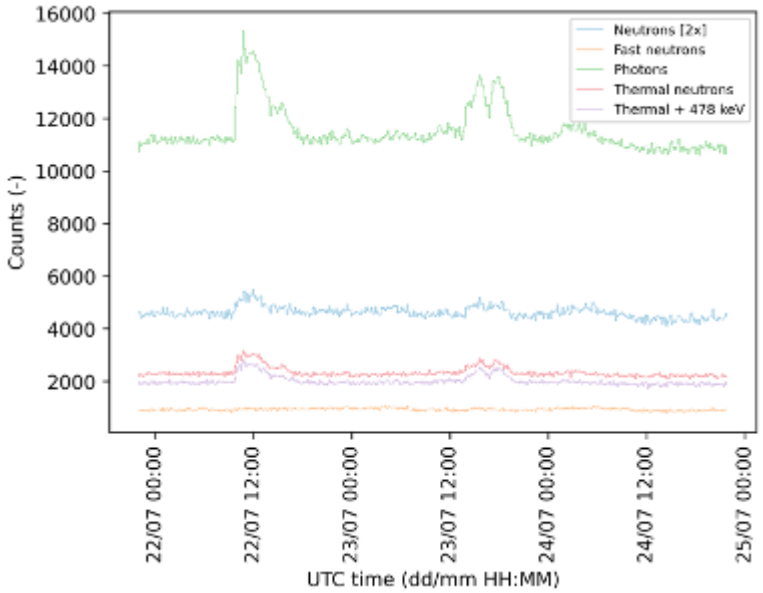

Figure 3.9 *The example of time series data from a neutron detector. The fast neutrons are neutrons with energies higher than 2 MeV*.

At Lomnický Štít there is also a SEVAN detector which continuously measures the cosmic radiation. This enabled us to compare the data between the neutron detector and the middle channel (plastic scintillator with a thickness of 25 cm) of the SEVAN detector, which is specifically designed to measure fast neutrons. In Figure 3.10 the comparison between SEVAN middle channel data and neutron detector data is shown for both detectors. The depicted period is two days. It can be seen that the fast neutrons (>2 MeV) measured by the neutron detector correlate with the SEVAN middle channel.

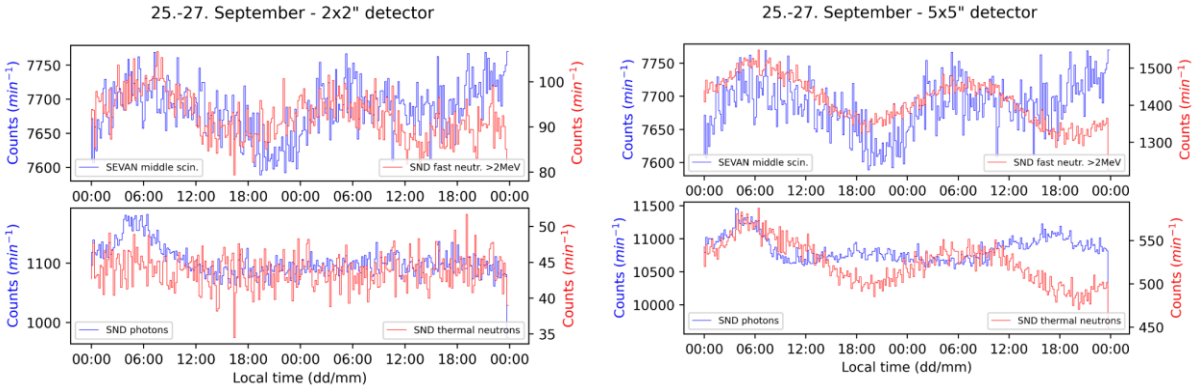

Figure 3.10 *The comparison of 2x2" (left) and 5x5" (right) neutron detector measurement with the SEVAN detector. For comparison, the bottom plots present thermal neutron and photon components measured by the neutron scintillation detectors*.

4 Detection efficiency of Timepix3 Stack Telescope detectors for thermal and fast neutrons

4.1 Purpose and introduction

In this project we developed a customized compact device (3 x 3 x 11 cm^3) high-resolution particle telescope consisting of two Timepix3 pixel detectors (each containing 65,536 pixels) arranged in close stacked architecture. Operating and reading out in synchronization, this design allows simultaneous measurement of deposited energy and time of arrival for individual particles in two pixel detectors – a top tracker, and a bottom tracker – with registration in sync (< 100 ns time window between both Timepix3 detectors, with a time resolution of 1.56 ns for a single chip). The resulting angular resolution for particle tracking is improved to < 1°. Exploiting quantum imaging sensitivity, per-pixel spectrometry for particle-deposited energy and wide-range tracking of charged particles (no collimators needed) with enhanced discrimination. The Timepix3 telescope tracker enables to precisely measure and monitor the flux, composition, and direction of mixed-radiation fields. We developed the device detection response methodology and carried out calibrations in reference fields for the newly developed device configuration customized for cosmic ray detection for the BIOSPHERE project based on Timepix3 technology. The detection efficiency constants for neutrons are derived based on measurements in reference thermal and fast neutron fields performed at the Czech Metrology Institute (CMI).

4.2 The Radiation Detector Stack Telescope Minipix Timepix3

The detectors are designed and built by ADVACAM. The Timepix3 ASIC chips are e developed within the Medipix Collaboration at CERN. The ASIC read–out chip contains a matrix of 256 × 256 pixels (total 65536 independent channels, where one-pixel size corresponds to 55 × 55 μm^2) and an active sensor area of 14.08 mm × 14.08 mm for a total sensitive area of 1.98 cm^2. Timepix3 provides two signal channels per pixel which can be set in various modes such as energy and counting, or energy and time of interaction at the pixel level. The Timepix3 detector is position, energy and time sensitive. For each ionizing particle (e.g. X-ray photon) it

digitally registers its position, energy, time of arrival and track shape. The other measures can be calculated from the track shape (particle type, direction of flight, charge, etc) (Oancea et al 2023). The information on each detected particle is either read out immediately (pixel mode) at a maximal rate of 2.3 million hit pixels per second (pixel mode) or accumulated in images (frame mode) and read out later at a maximal speed of 16 frames per second. Advacam developed and calibrated two customized particle trackers that consist of 2 synchronized Timepix3 detectors configured into a compact stack particle tracker.

Two customized configurations have been developed: A prototype *MiniPIX-TPX3 telescope, prototype detector,* is equipped with a silicon sensor 300 µm thick (top TPX3 tracker) and a 1000 µm thick Si sensor (bottom TPX3 tracker) (Granja,2022) referred to as Stack #1. The spacing distance between the top and bottom trackers is 10 mm. Stack #1 was customized with a neutron converter mask (see Sec. 3) mounted on the bottom tracker.

The customized *MiniPIX-TPX3 telescope,* is equipped with a silicon sensor of 500 µm thick (top TPX3 tracker) and a 2000 µm thick CdTe sensor (bottom TPX3 tracker) referred to as Stack #2. Stack#2 had customized **i) sensor material**: for the bottom tracker with a thick (2000 µm) CdTe sensor is used for increased detection efficiency of X rays and low-energy gamma rays and **ii) the gap distance** between the detector trackers: 10 mm in Stack #1 and 4 mm in Stack #2. The thickness of the detector sensors is also different. This architecture enables measurement of the energy loss of single particles in two different sensors with registration in sync (< 100 ns time window between both Timepix3 detectors). The customized Stack #2 device is shown in Figure 4.1.

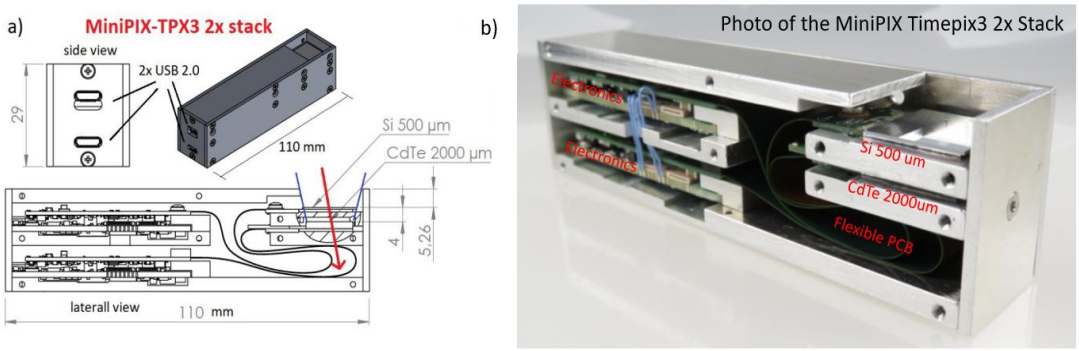

Figure 4.1 *The miniaturized particle telescope MiniPIX-Timepix3 2x Stack with Si and CdTe sensors: (a) Integrated architecture and dimensions with 4 mm spacing gap between the top (500 µm Si) and bottom (2000 µm CdTe) trackers. The synchronized detection of a charged particle (in red) and the telescope field-of-view (in blue) are indicated. b) Assembled device readout by two USB 2.0 cables to standard PC.*

The TPX3-based device is controlled and readout via USB2.0 interface with a standard USB connector (service port) using the PIXET software package. The devices operate at room temperature. Limited e.g. passive cooling is recommended.

4.3 Per-Pixel energy calibration

For the Timepix3 detectors in the Stack Minipix Telescopes the per-pixel energy calibration (Jakubek 2011) makes use of discrete-energy X-ray fluorescence photons (XRF) e.g. from In (24.7 keV) and low-energy gamma rays from radionuclide sources ^{55}Fe (5.9 keV) and ^{241}Am (59.5 keV). the resulting spectral response range is from 5 keV to over 1000 keV per pixel. The charge sharing effect enables to register the deposited energy of single particles up to tens of MeV in the semiconductor sensor material.

4.4 Neutron converter mask

Figure 4.2 shows a single-chip Minipix Timepix3 detector equipped with thermal and fast neutron converters (Granja, 2023). For thermal neutron detection is used ^{6}Li and for fast neutron detection plastic e.g. PE-material.

In addition, there are also direct fast neutron-induced interactions in the detector Si sensor material. Figure 4.2b shows a radiography of the detector with neutron converter masks.

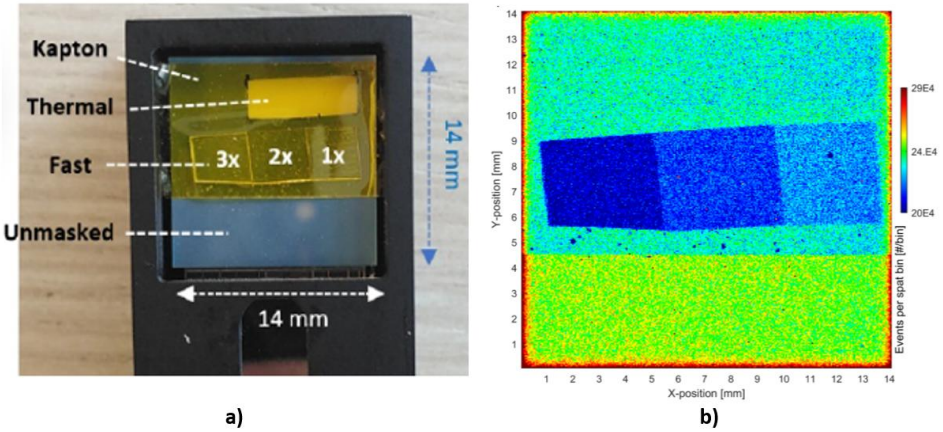

Figure 4.2. ***a)*** *The Minipix Timepix3 detector with converters for thermal neutrons (LiF) and fast neutrons (PE-material (Granja, 2023).* ***b)*** *X-ray radiography of the detector mask. The entire sensor area is shown = 256 × 256 pixels = 14.08 mm × 14.08 mm = 1.98 cm².*

4.5 Measurements in metrology Neutron Fields at CMI

Experiments were carried out at the CMI facility to characterize and calibrate the detection efficiency for fast neutrons from AmBe (Fig. 4.3a) and for thermal neutrons from a thermal neutron pile (Fig. 4.3b).

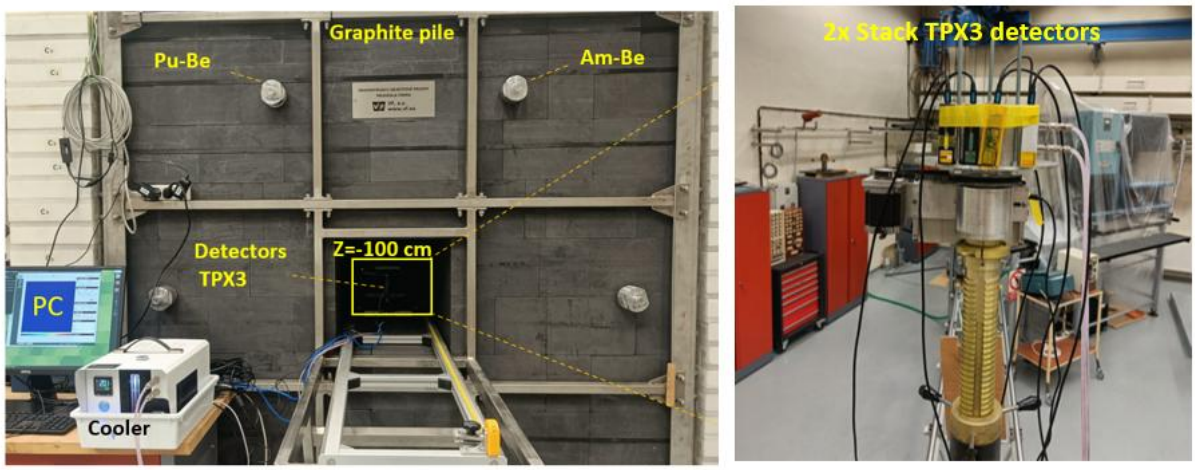

Figure 4.3. *Experimental setup at the CMI facility in Prague: a) The thermal neutron graphite pile with radionuclide neutron sources Am-Be and Pu-Be, b) fast neutron field broad spectrum from Am-Be source.*

4.6 Calibration at reference thermal neutron field at the graphite pile

The calibration of the detectors with individual converters was performed at the Czech Metrology Institute which uses a graphite pile (Vykydal, Králík 2018) to maintain a reference thermal neutron field for metrology and dosimetry purposes. It consists of three Pu–Be and three Am–Be radionuclide sources positioned in a star

pattern inside a 1.95×1.95×2.0 m^3 (width, length, height) graphite moderator block as illustrated in Figure 4.3a. The pile has an experimental channel in its center with dimensions of 40×40×135 cm^3 (width, length, depth). The calibration measurements were carried out at the reference point inside the pile. The reference thermal neutron fluence rate (isotropic field) was Φ_{ref} = 2.91(5) × 10^4 $cm^{-2}{\cdot}s^{-1}$ (Vykydal, Králík 2018), the uncertainty (number in brackets following a reported value) is given for k=1. The following formula was used to calculate the thermal neutron detection efficiency, η , for each pair of detector-converter:

$$\eta 1 = \frac{N_a}{\Phi_{ref}}, \quad (1)$$

$$\eta 2 = \frac{N_b}{\Phi_{ref}}, \quad (2)$$

where N_a is the total number of clusters/particles measured and N_b is the number of circular clusters measured under the ^{6}LiF converter initiated by thermal neutron interactions (clusters particles $cm^{-2}{\cdot}s^{-1}$), (Oancea et al 2023a).

The data acquired during the calibration of the Timepix3 detector in the thermal neutron pile using the ^{6}LiF converter are displayed in Figure 4.4b (Stack#1) and Figure 4.4c (Stack#2). The per-pixel deposited energy displayed in color logarithmic scale with an illustration of the region where the ^{6}LiF converter was placed on the right region can be seen, whereas the bottom of the figure contains only the background radiation. To calculate $\eta 2$, only the region below the thermal neutron converter was considered for the graphite pile measurements. In the area with the converter, specific circular tracks are seen which are created by the interaction of neutrons with ^{6}LiF and the emission of alpha and tritium particles. A machine learning algorithm was used to distinguish the high-energy tracks created by products of thermal neutron interactions (circular tracks) in the converter and to calculate the detection efficiency of each detector-converter pair. In this work two classes of particles were identified: i) circular tracks and ii) photons.

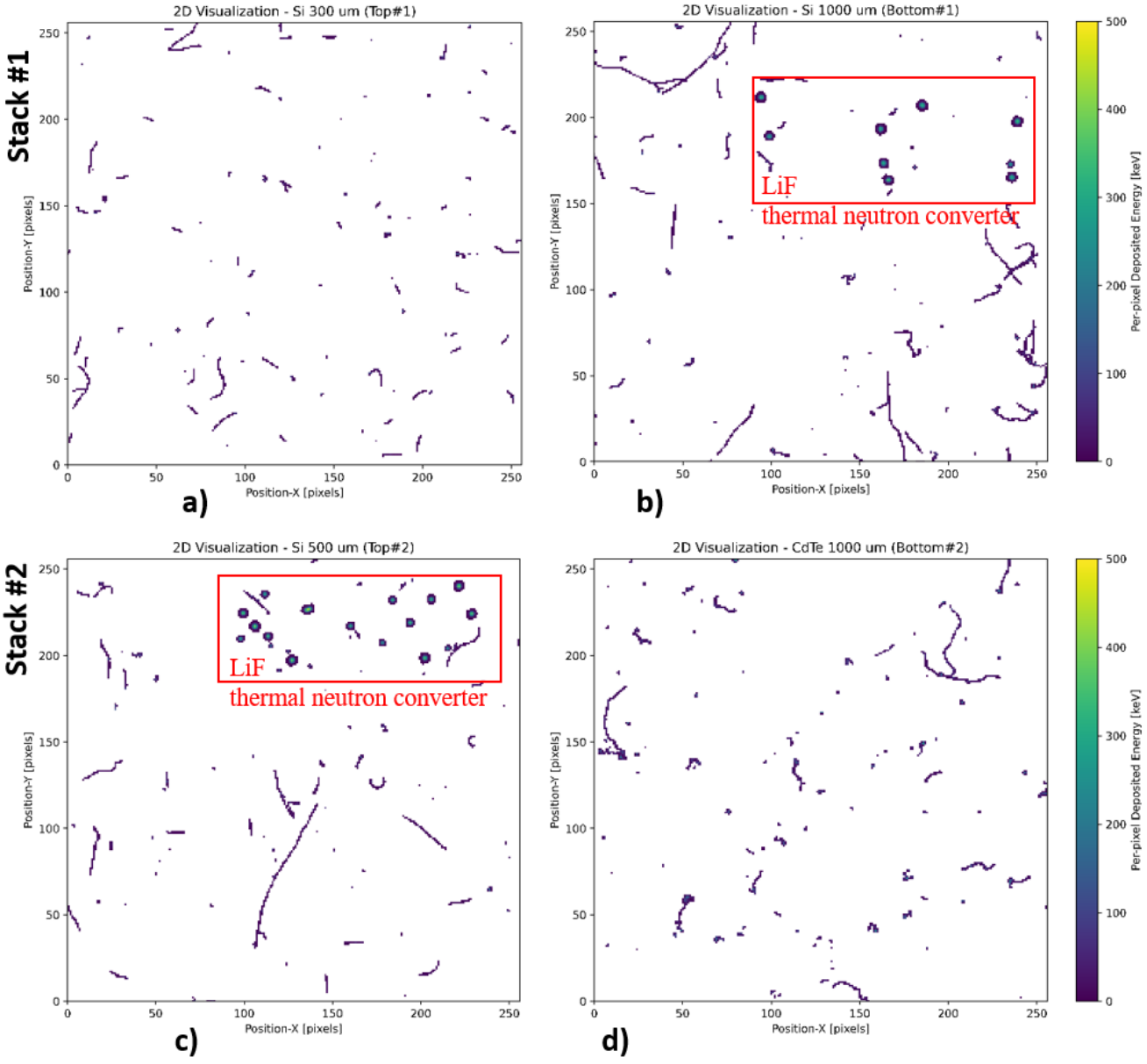

Figure 4.4. *Detection and radiation field visualization by Timepix3 of thermal neutrons from Stack #1 (top) with a) top tracker Si sensor 300 µm and b) bottom tracker Si sensor 1000 µm. The region of the LiF converter is emphasized with a red square. On the bottom figure are presented data from Stack #2 with c) top tracker Si sensor 500 µm and d) bottom tracker CdTe sensor 1000 µm. The regions of the thermal neutron converter mask are highlighted. The per-pixel deposited energy is shown by the color bar scale. The full detector pixel matrix is displayed (256 × 256 pixels = 14.08 mm × 14.08 mm = 1.98 cm^2 = 65.536 pixels). Data was collected in about 1s. 100 particles are displayed in each image.*

4.7 Fast neutron interactions in the silicon sensor and in the converter mask

The silicon material in the sensor itself is sensitive to fast neutrons in a broad range of energy (Granja, 2022). This results in the detector response to neutrons across all mask regions including the unmasked region. Neutron interactions in silicon are due to direct nuclear reactions such as (n,α) and (n,p) on ^{28}Si. The emitted reaction products consist of protons and alpha particles which interact and are detected in the silicon sensor itself. Additional neutron-induced interactions include further detection channels such as elastic scattering

and nonionizing interactions directly also on the silicon matrix of the sensor (Granja et al 2023). These processes are expected to occur homogeneously over the entire sensor. The resulting detection component will manifest in the unmask region and appear superposed to all other regions. Figure 4.5 illustrates the radiation field detected in all areas of the detector. The impact of the fast neutron masks is not seen as compared to the unmasked region, so the detection efficiency is calculated for the entire sensor area. The reference fast neutron field at the detector's position was given as Φ_{ref} =4.48 E3 ± 1.3% particles cm $^{-2}$·s $^{-1}$, at a distance of 20 cm and Φ_{ref} =4.07 E3 ± 1.3% particles cm $^{-2}$·s $^{-1}$, at a distance of 21 cm from the AmBe source.

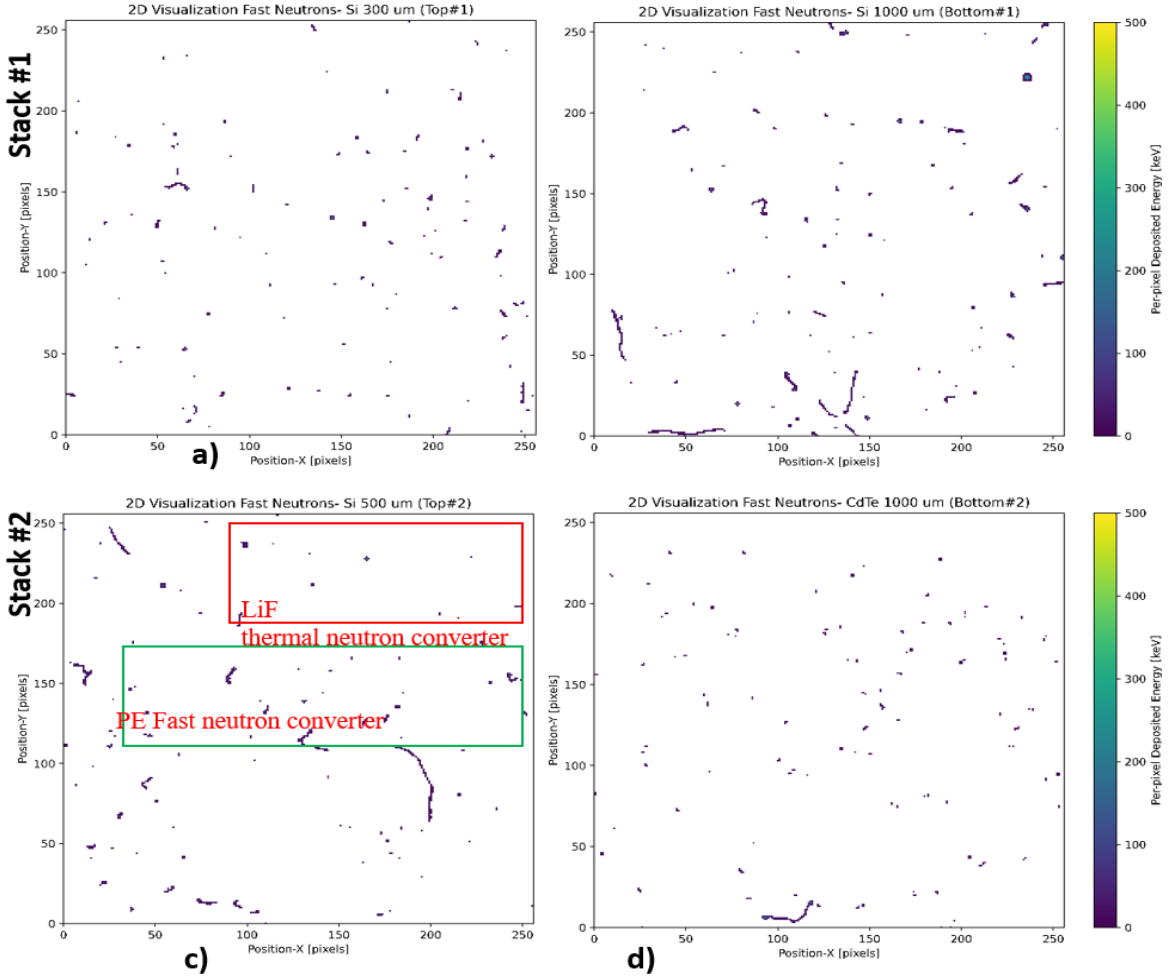

Figure 4.5. *Same as Figure 4.4 showing the detection and radiation field visualization by Timepix3 to fast neutrons from the AmBe source. 100 particles are displayed in each figure.*

4.8 Monte Carlo simulations

Monte Carlo (MC) simulations were performed using a general-purpose MC code MCNP version 6.2 (Werner et al.). The simulations used electron-photon relaxation library EPRDATA14, electron library el03, proton library ENDF/B-VII.0, photonuclear reaction library ENDF/B-VII.0, and neutron library ENDF/B-VIII.0 at 293.6 K. The MC model of the stack telescope detector consisted of sensor and readout elements of appropriate

thickness and material, printed circuit board (simplified), holders, and a metal box with an entrance window (Figure 4.6).

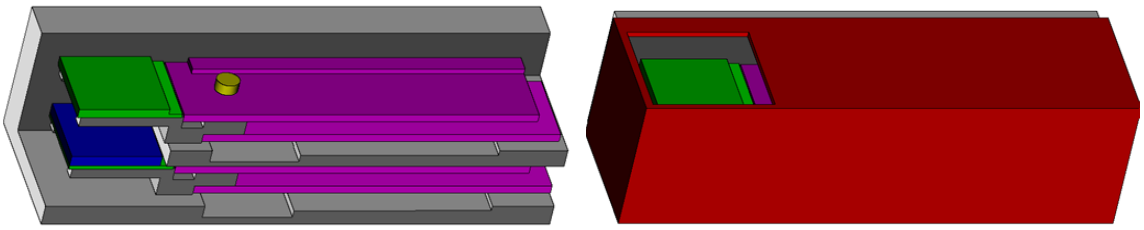

Figure 4.6. *Visualization of the MC model of the miniaturized particle telescope MiniPIX-Timepix3 stack with a 500 um Si sensor (top TPX tracker) and a 2000 um CdTe sensor (bottom TPX3 tracker).*

The conversion layers for the detection of thermal and fast neutrons were included in the model. Because the thickness and exact isotopic composition of the ^{6}LiF conversion layer changes detector-by-detector, the thickness was varied until an agreement of the simulated and measured detection efficiency for thermal neutrons was obtained. The simulations for thermal neutrons took into account neutrons only, neglecting the photons. The source was isotropic and the energy distribution was obtained from other MC simulations done at CMI. On the other hand, the simulations for the AmBe fast neutron source assumed a parallel wide neutron beam with the energy distribution taken from ISO 8529-1:2001.

The scored quantity was the number of counts generated by different types of charged particles in the sensor area below each converter. For determination of thermal neutron detection efficiency, only counts caused by alpha and triton particles originated in ^{6}Li disintegration were used. Fast neutron detection efficiency was obtained from counts caused by protons originated in the PE converter. For a more detailed future study, mesh tallies with 256x256 elements were constructed for storing and visualization of particle tracks in the pixels.

4.9 Results: Energy spectra, particle flux, and deposited energy

4.9.1.1 Flux of particles

Figure 4.7 shows of the measured particle flux for distinct sensor-material-thickness configurations by both telescope systems (stack #1 and stack #2). The measurements include all recorded particles in the detector's sensor, providing a detailed assessment of the system's performance under varying conditions. In Figure 4.7a, the particle flux in a thermal neutron pile is presented, defining the influence of different sensor configurations. Specifically, Stack#1 contains a top sensor with a thickness of 300 µm of silicon and a bottom sensor with a thickness of 1000 µm, while Stack#2 features a top sensor with a thickness of 500 µm of silicon and a bottom sensor with a thickness of 1000 µm CdTe. This comparison of particle flux in the context of thermal neutron conditions shows a higher detection for the CdTe sensor material for photons created inside the thermal neutron pile. Figure 4.7b shows the flux in fast neutron fields (AmBe) for Stack#1 and Stack#2. The total particle flux measured in each configuration serves as a fundamental parameter for deriving the detection efficiency. This quantification of particle flux under diverse conditions is important for evaluating and optimizing the detector's capability to detect and quantify neutron particles accurately.

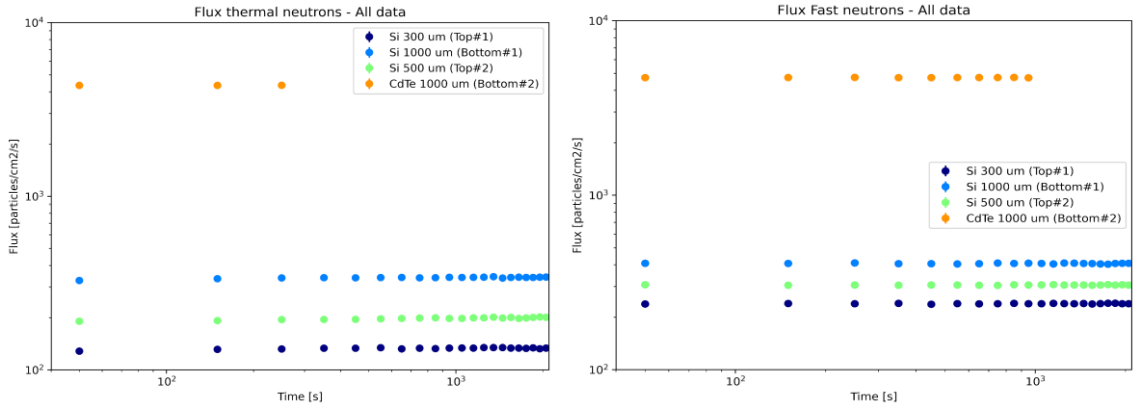

a) **b)**

Figure 4.7. *The flux of particles was measured for **all particles** in each of the TPX3 detectors in both telescopes. a) Particle flux in thermal neutron pile and b) flux in Fast neutron fields (AmBe) measured in the following sensor-material-thickness configurations: Stack#1: Si 300 um (top) and Si 1000 um (bottom), Stack#2: Si 500 um (top) and 1000 um (bottom).*

Each stack contained a region with a LiF thermal neutron converter, where besides photons were detected circular tracks specific for thermal neutron interactions with the converter and emission of tritium and alpha particles. Using a machine learning algorithm, the thermal neutron interactions were separated from background radiation and the results are displayed in Figure 4.8. The tracks below the thermal neutron converter for Stack#1, where the converter was placed on the bottom layer of the detector are shown with orange color. For Stack#2, where the detector was placed on the top layer, flux from circular tracks is shown with red color. Furthermore, the flux below the converter is used to calculate the detection efficiency and it is displayed in Table 1 as $\eta 2$.

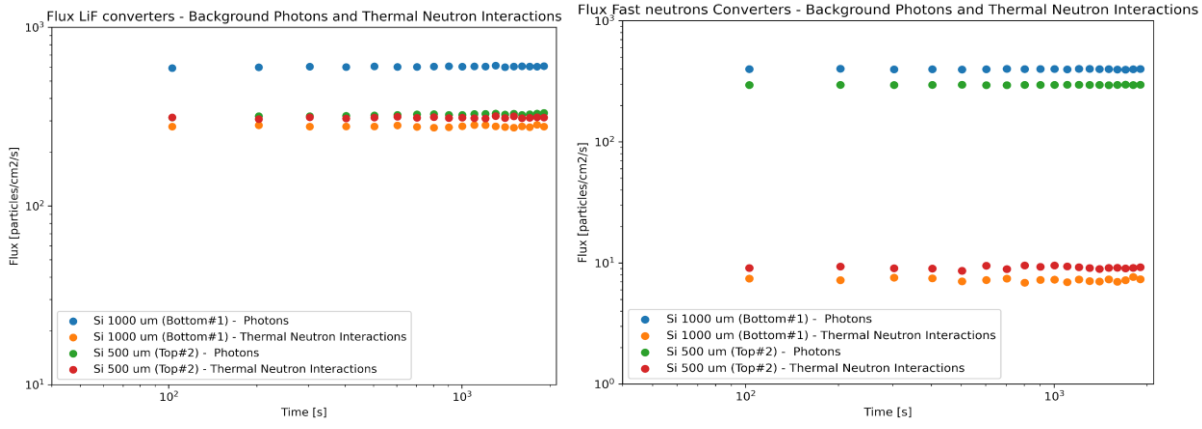

b) **b)**

Figure 4.8. Same as Fig. 4.7 for *the measured flux of selected particles sorted into two classes: **as photons and thermal neutron** interactions (circular tracks) in the detector's sensor. Particle flux for the two detector's layers which contained LiF thermal neutron converter measured in the following sensor-material-thickness configurations: Stack#1: Si 1000 um (bottom), Stack#2: Si 500 um (top). Data measured in a) thermal neutron pile and in b) fast neutron source: AmBe.*

4.9.1.2 Neutron detection efficiency

The neutron detection efficiencies obtained for all investigated chip-sensor configurations are summarized in Table **1**. The detector has 100 % detection efficiency for charged particles, but it has limited detection for neutrons.

Table 1 provides an overview of the A) thermal neutrons and B) fast neutrons detection efficiency, symbolized as η, for Timepix3 detectors. The presented values are specific to each calibrated detector and incorporate uncertainties originating from both statistical aspects and the reference thermal neutron flux. The notation η (1) signifies the detection efficiency under direct reaction in the sensor including all particles, while η (2) reflects the detection efficiency when utilizing thermal neutron converters. The detection efficiency for the detectors equipped with a thermal neutron converter (based on circular tracks) was around 1 %, whereas if accounted for all particles the detection efficiency is higher in the CdTe sensor as compared to the sensors manufactured from Si. In the fast neutron field, the detection is higher than 100% due to the detection of generated gamma radiation and the high sensitivity of the detector.

Table 1. A) Thermal neutron and B) fast neutron detection efficiency, η, for Timepix3 detectors for direct reaction in the sensor η (1) and with thermal neutron converters η (2). Values are given for each calibrated detector.

A. Thermal neutrons

Detector sensor, thickness, ID	η (1) [%]	η (2) [%]
Si 300 um (Top#1), TPX3 M(	0.46 ± 0.004	-
Si 1000 um (Bottom#1), TPX3 I05	2.07 ± 0.002	0.096 ± 0.002
Si 500 um (Top#2), TPX3 D05	1.11 ± 0.002	1.074 ± 0.002
CdTe 1000 um (Bottom#2), TPX3 D04	14.97 ± 0.013	-

B. Fast neutrons

Detector sensor, thickness, ID	η **(1) [%]**	η **(2*) [%]**
Si 300 um (Top#1), TPX3M07	5.88 ± 0.01	-
Si 1000 um (Bottom#1), TPX3 I05	9.10 ±0.01	0.180 ± 0.001
Si 500 um (Top#2), TPX3 D05	7.52 ± 0.01	0.200 ± 0.001
CdTe 1000 um (Bottom#2), TPX3 D04	105.55 ± 0.04	-

(1) Obtained from all particles including photons;
(2) Obtained from circular tracks only under converter;
(2*) Obtained from circular tracks in all area detector;

4.9.1.3 Performance of the Stack detector

Figure 4.9 presents histograms detailing the deposited energy distribution in both thermal and fast neutron fields across various sensor-detector configurations. The histograms include data from all detected particles, providing a comprehensive overview of the energy deposition in the interval from 3 keV the minimal threshold to over 3 500 keV, covering a wide range of energy.

In Figure 4.9a, the histogram illustrates the distribution of deposited energy in thermal neutron fields. This allows for an examination of how different sensor-detector configurations influence the energy deposition patterns of particles, especially below the thermal neutron converter. The emitted alpha and tritium particles below the converter are highly energetic particles, having a peak in the energy interval 1800-2400 keV (see yellow and green colors). On the other hand, photons are low-energy particles and are detected with higher detection efficiency in the CdTe sensor.

Figure 4.9b displays the histogram of deposited energy in a fast neutron field where mostly low-E particles were created in the sensor. The thermal neutron component is absent in the energy spectra, where circular tracks were presented in low flux across the entire sensor surface.

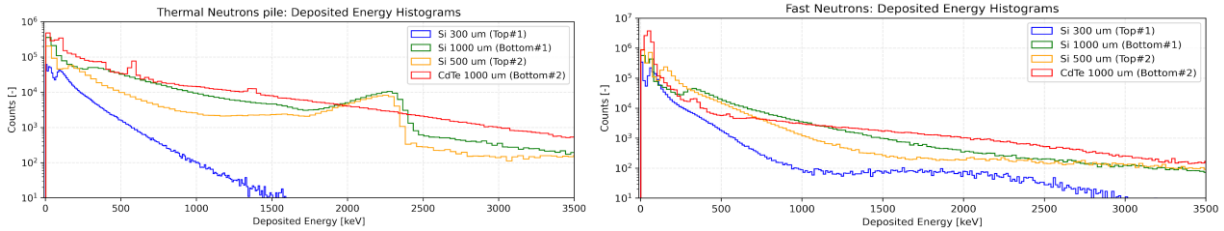

a) **b)**

Figure 4.9 *Deposited energy spectra in a) thermal and b) fast neutron fields for all sensor-detector configurations. Data shown for all detected particles.*

4.10 Summary

We tested and evaluated the response of the Timepix3 detectors with silicon and CdTe sensors to thermal and fast neutrons produced in well-defined reference radiation fields in terms of radiation field visualization, flux, detection efficiency and neutron energy. Results are produced for the various detector-sensor and the various mask-regions configurations used together with selective individual particle event type classes. The latter tool improves the neutron detection selectivity and enhances the discrimination of background and unwanted events. The neutron detection efficiency is provided for each sensor-detector-converter configuration.

5 Adaptation and upgrade of a LIDAR system for vertical profiling of atmospheric temperature, density, and aerosols

5.1 Introduction

The Light Detection and Ranging (lidar) technique is able to retrieve the range-resolved vertical profile of atmospheric parameters (i.e. density, pressure, temperature, wind, etc.) along with that of gases (e.g., water vapor) and aerosols. A typical lidar system consists of two units: the transmitter (laser system) and the receiver (optical and opto-electronic subsystems (Figure 5.1). To measure the aerosol vertical profile pulsed laser systems are used emitting in the UV up to NIR regions (355-2000 nm), while to obtain the atmospheric density profile lasers at 532 nm are mainly used.

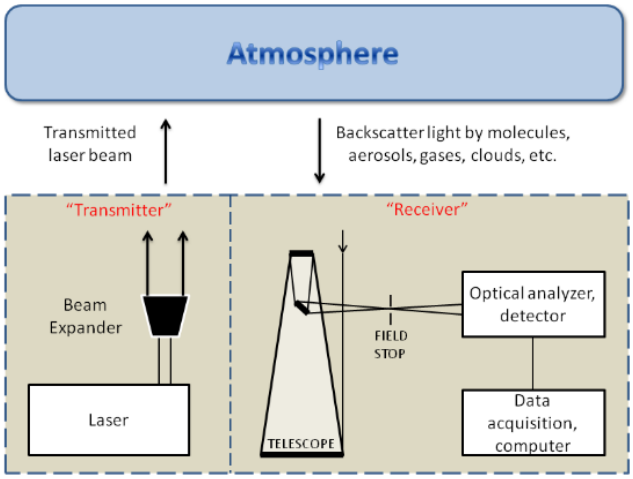

Figure 5.1. *General lidar system schematic configuration (Weitkamp, 2005).*

During daytime the aerosol vertical profiles are obtained using the Mie elastic backscattering technique based on Klett (1981, 1983), while during nighttime, in addition to Mie scattering, the Raman scattering by the atmospheric N_2 is used to mimize the aerosol optical properties (a_{aer} extinction and b_{aer} backscatter coefficients) and mass concentration, retrievals. At the National Technical University of Athens (NTUA) the EOLE lidar system provides the vertical profiles of a_{aer}, b_{aer}, as well as the aerosol mass concentration (the latter only in aerosol-free atmospheric layers). The EOLE's detection range spans from 0.8 to 8-10 km with a measurement accuracy of the α_{aer} and β_{aer} , in the range 10-15 % to 10-25 %, with spatial resolution of 30 m (800 m height) and 100-250 m (8-10 km height) (Kokkalis et al., 2021) (Figure 5.2).

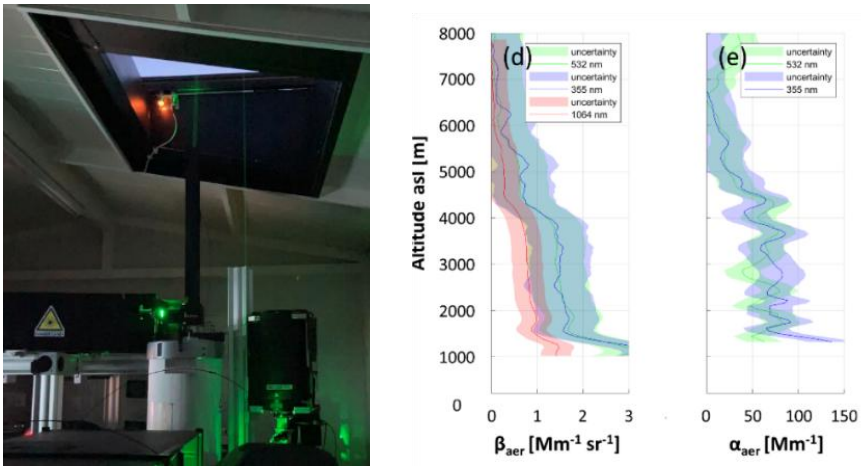

Figure 5.2. *Left: The EOLE lidar system; Right: Vertical distribution of aerosol optical properties at 355-532-1064 nm obtained by the EOLE lidar over Athens (Kokkalis et al., 2021).*

Moreover, the atmospheric density profile is possible to be retrieved by using the elastic Rayleigh backscattering from the atmospheric molecules only in aerosol-free atmospheres (mostly over 4-5 km asl. heights) (Weitkamp. 2005). A typical atmospheric density profile (green line) obtained by EOLE is shown in Figure 5.3, as compared to the local radiosonde data (red line); the lidar density profile is valid only in the aerosol-free region (5-25 km).

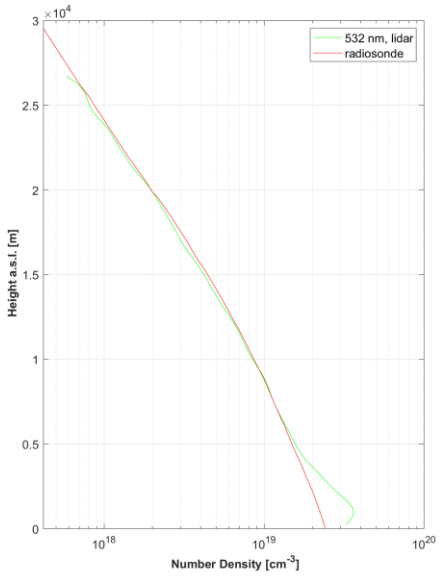

Figure 5.3: *Typical atmospheric density profile (green line) obtained by EOLE lidar, as compared to the local radiosonde data (red line); the lidar density profile is valid only in the aerosol-free region (5-25 km).*

Aerosol mass concentration profiles have been obtained during the last years based on aerosol vertical profiles of a_{aer} and the particle depolarization ratio, using the POLIPHON technique, which permits the retrieval of the particle number, surface area, and volume concentration for dust and non-dust aerosol components (Ansmann et al., 2011), as shown in Figure 5.4.

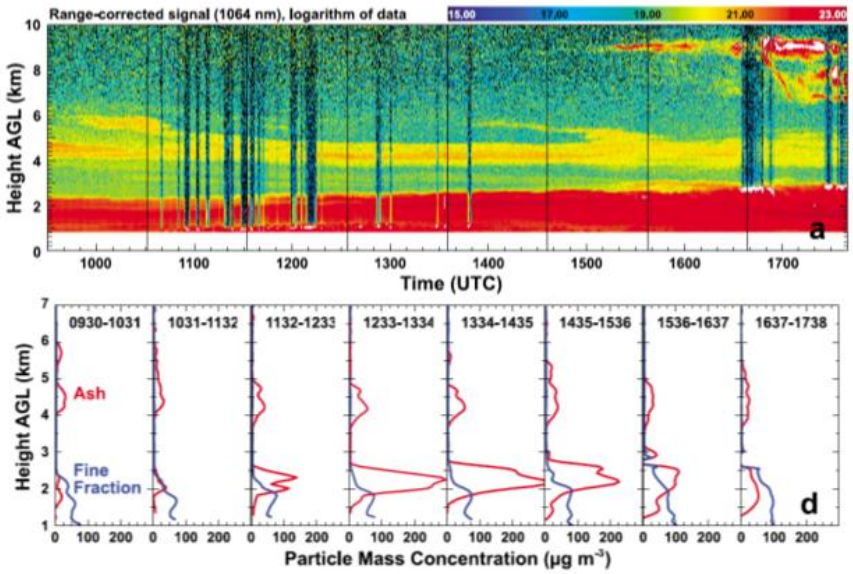

Figure 5.4 *(a) Height-time display of the 1064 nm range-corrected signal measured at Leipzig on 19 April 2010) and 1 h mean profiles of (d) fine-fraction (blue) and ash (red) mass concentrations determined from the backscatter coefficients after cloud screening (Ansmann et al., 2011).*

Atmospheric temperature profiles were first obtained in 1972 (Cooney, 1972) using the rotational Raman spectrum (RRS) of laser light backscattered by atmospheric N_2 and O_2. Since the energy distribution between the spectral lines in the RRS depends on temperature, by measuring the ratio of the laser scattered power between two spectrally close lines of the RRS the temperature may be deduced. Temperature profiles retrieved by this method and using narrow-band interference filters (IFFs) are confined from ground to the upper stratosphere.

The temperature lidar system of Raymetrics SA is currently capable of detecting lidar signals at 5 channels (354.78nm, 387nm, 407nm and at two PRR channels (355.4 nm, 356.3 nm), the latter used to retrieve the atmospheric temperature profiles (Reichardt et al., 2012). The lidar signals at the two PRR channels are confined with interference filters (IFFs) with FWHM of 0.25 nm (T=25% peak) and 0.6 nm (T=60%), respectively (Figure 5.5). The lidar system provides vertical temperature profiles from 500 m up to 3.5-4 km during daytime and 18-19 km during nighttime, under favorable meteorological conditions (e.g. no clouds, low aerosol content).

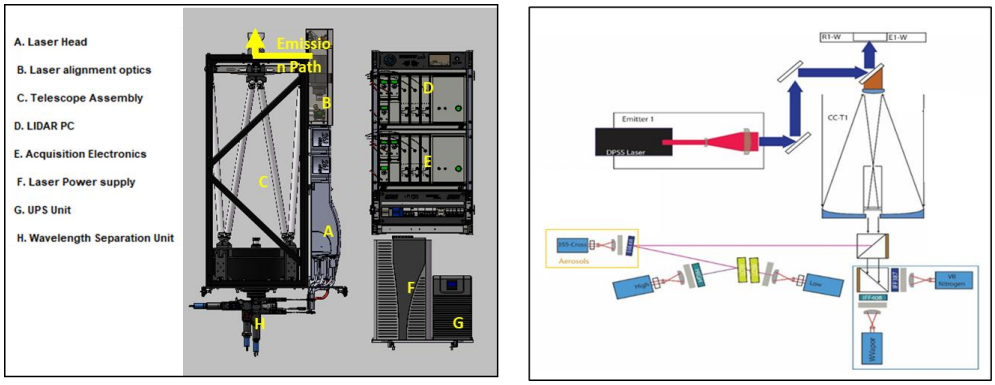

Figure 5.5 *Schematic representation of Raymetrics temperature lidar system (left) with ist optical path (right).*

Figure 5.6 presents two typical temperature profiles obtained over Athens during daytime (left) on 18 September 2019 (spatial resolution 90 m, temporal resolution 15 min), and nighttime on 5 September 2019 (spatial resolution 900 m, temporal resolution 85 min), compared to model profiles (red line, right figure).

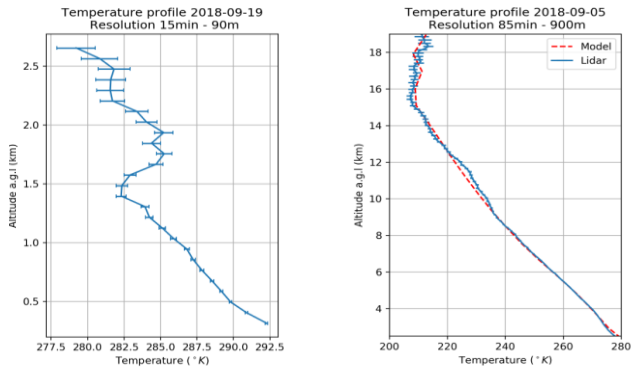

Figure 5.6. *Typical temperature profiles obtained over Athens by the Raymetrics temperature lidar; left: daytime measurements (18 September 2019) with a spatial resolution of 90 m and temporal resolution of 15 min, right: nighttime measurements (5 September 2019) with a spatial resolution of 900 m and temporal resolution of 85 min, compared to model profiles.*

5.2 Characterization of the LIDAR systems used in BIOSPHERE

To reach the specifications of BIOSPHERE (e.g. temperature profiling up to 22-25 km with 1K accuracy, 1 min temporal resolution; atmospheric density and aerosol mass concentration accuracy better than 10% up to 25 km with 15-30 min temporal resolution) an upgrading of the lidar systems has been discussed. The upgrading of a lidar system can be achieved in two ways: either by scaling up the power of the emitting laser source to obtain a stronger lidar signal, or by upgrading the receiving system to reduce, as much as possible, the atmospheric background, which is considered as noise.

The technical characteristics of the NTUA EOLE lidar system comprise a pulsed Nd:YAG laser system which emits, simultaneously, laser pulses at 354.93-532-1064.2 nm, with energies of 240-310-260 mJ, respectively, at 10 Hz repetition frequency. A Cassegrainian telescope of 300 mm diameter (focal length 600 mm) collects all elastically backscattered lidar signals (354.93-532-1064.2 nm), as well as those generated by the spontaneous vibrational-rotational Raman effect (by atmospheric N_2 at 386.6 and 607.4 nm, as well as by H_2O at 407.5 nm), within a field of view of 1.5 mrad. To upgrade the EOLE lidar one more lidar channel at 1064 nm could added to provide aerosol depolarization data at 1064 nm with an accuracy of 10-30 % (Haarig, et al., 2018). To increase the maximum measurement height above 20 km (for both aerosols and air density measurements), the laser energy of the lidar should be increased to 800-1000 mJ/pulse at 532 and 1064 nm, respectively, with a repetition rate of 30 Hz (Baars, et al., 2019; Haarig, et al., 2022) and an increase of the telescope diameter from 300 to 400 mm. However, due to the limited budget of BIOSPHERE such a hardware upgrade was not possible.

The monoaxial Raymetrics temperature lidar system is equipped with a Single Longitudinal Mode (SLM) Nd:YAG laser, emitting 200mJ/pulse at 354.7 nm, with 10 Hz repetition rate and 6-8 ns laser pulse duration. The Cassegrainean receiving telescope has a diameter of 400 mm and *f* number =10. Its field of view can be adjusted from 0.25 mrad up to 1 mrad. To extend the measurement range of the lidar system above 20 km, it was suggested to increase the energy at 354.7 nm up to 400–500 mJ/pulse at 30 Hz repetition rate. Additionally, a beam could be added to reduce the laser beam divergence to ≤0.1 mrad (full angle) and to guarantee eye-safety (if needed). Furthermore, a second 200 mm diameter telescope (FOV=3.2 mrad) could be synergistically used, to decrease the minimum range to less than 0.3 km. However, due to the limited budget of BIOSPHERE such a hardware upgrade was not possible.

The hardware low-cost upgrades implemented at the Raymetrics lidar system included: i) the adjustment of the receiving telescope FOV to reduce the atmospheric background radiation entering the telescope, thus, improving the signal-to-noie ratio (SNR) of the lidar signal, ii) the installation of sliding neutral density (ND) optical filter modules, ii) addition of narrow band filters (NBF) used to transmit the lidar signal onto the PMTs and reject all other wavelengths.

Further to the hardware upgrades, software upgrades were implemented at both lidar systems, as follows: i) NTUA lidar: new format of the NTUA lidar signal data was used to feed the Single Calculus Chain (SSC) (D'Amico, et al., 2015a,b; Mattis, et al., 2016) to retrieve the vertical profiles of the aerosol optical properties (a_{aer} and b_{aer}); development of a Matlab code to provide the vertical profiles of the mass concentration of dust and non-dust particles, as well as their total mass; development of a Matlab code to provide the vertical profiles of the atmospheric density based on NTUA elastic backscattered lidar vertical profiles at 532 nm and compared against local radiosonde profiles, from ground up to 20-25 km height, and ii) Raymetrics lidar: an analysis algorithm called "Raymetrics Lidar Workstation" was developed as a web-based application, capable of analysing and displaying

lidar data complemented with data from auxiliary sensors. Its main purpose is to provide semi-real time lidar data products, semi-real time suxiliary sensors data, and data archive which allows the user to filter and display older lidar data.

5.3 Performance of LIDAR system with respect to system for vertical atmospheric profiling parameters

The performance of the NTUA EOLE lidar system regarding the vertical profiling of the atmospheric density can be verified by comparing the EOLE lidar data to local radiosonde data which are the reference data for the atmospheric density, as shown in Figure 5.7. We can see that the lidar-derived density profile is valid only in the aerosol-free regions. Thus, the differences between the lidar and radiosonde data are of the order of <20% (from 5-8 km), and <5% (10-25 km), while, below 5 km the lidar-derived density profile is not accurate, as this height region contains large quantities of aerosols and is not an aerosol-free region.

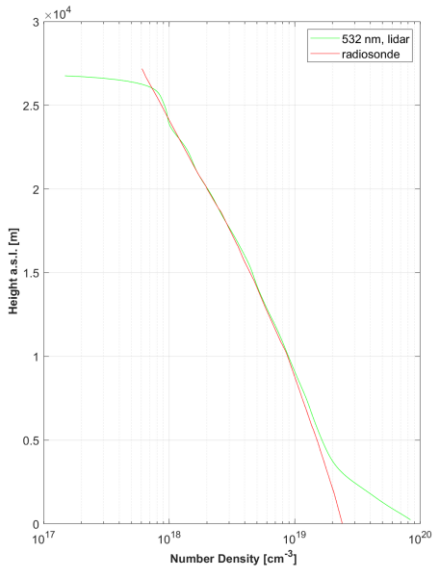

Figure 5.7: *Atmospheric density profile (green line) obtained by EOLE lidar over Athens on 06 July 2023, as compared to the local radiosonde data (red line).*

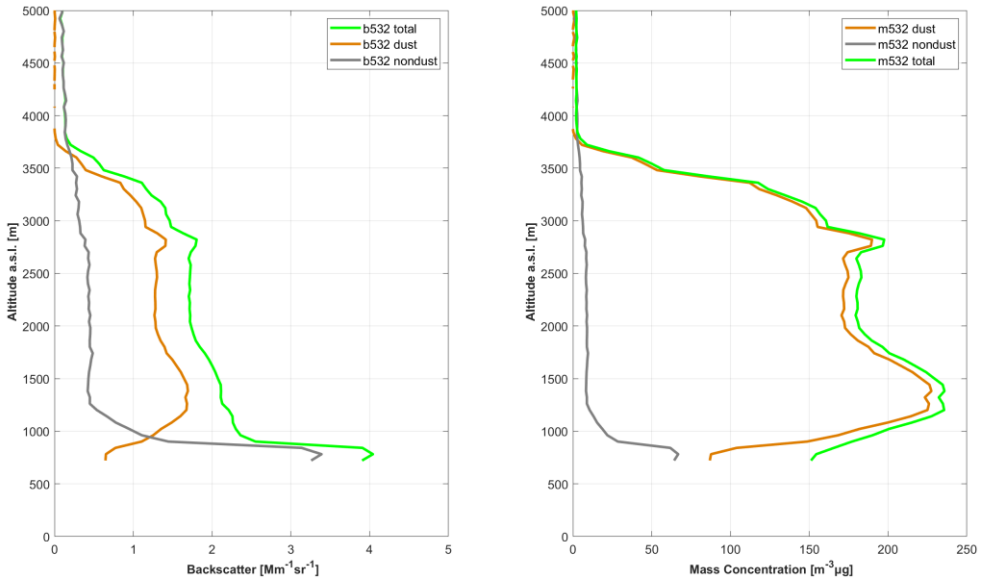

a) b)

Figure 5.8. *Vertical profiles of the aerosol a) backscatter coefficient (b_{aer}) at 532 nm and b) mass concentration derived from NTUA lidar measurements over Athens (16:31-17:33 UTC) on 24 October 2022.*

Concerning the profiling of the aerosol mass concentration up to the free troposphere, there is no certified conventional and available technique able to provide it. Here we present two examples of the aerosol backscatter coefficient (b_{aer}) and the relevant aerosol mass concentration at 532 nm derived from NTUA lidar measurement over Athens between (16:31-17:33 UTC) on 24 October 2022 (Figure 5.8). The orange lines represent the dust, the grey lines the non-dust aerosols, while the green lines represent the aerosol backscatter coefficient (left hand side graph) and the total aerosol mass concentration (right hand side graph) profiles.

The vertical profiling of the atmospheric temperature is obtained by the Raymetrics lidar during daytime and nighttime operation. Figure .9 shows the intercomparison of the radiosonde (black line) and lidar (green line) from 600-3800 m height during the daytime operation. A typical intercomparison between lidar and model data, for nighttime operation, is shown in Figure 5.6-right).

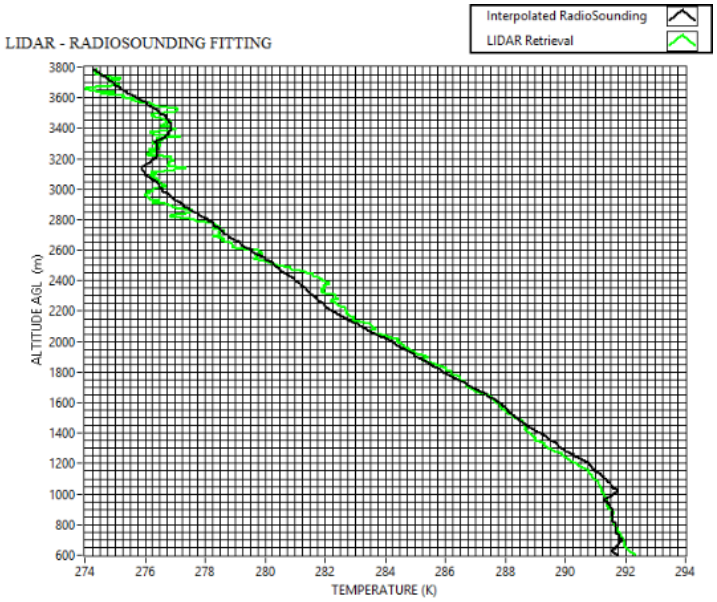

Figure 5.9. *Radiosondes-Lidar comparisons on 15.09.2019 at 11:00 UTC. The lidar profiles have been obtained by the Raymetrics lidar in the frame of the CROSSINN campaign at Innsbruck, Austria*.

5.4 Outlook: minimal and optimal measuring parameters and the technical requirements of an optimum LIDAR system

Based on actual bibliographical data (Haarig et al., 2018), the density profiles currently retrieved by the EOLE lidar are provided with an accuracy of 20 %, which after upgrading the energy of the emitted laser power and the receiving telescope diameter to 400 mm, is increased to 10-15 %. Additionally, the aerosol mass concentrations profiles retrieved, currently, by EOLE are provided with an accuracy of 20-30 % and after upgrading the energy of the emitted laser beam, the accuracy will be increased to 10-20 %. The range (and time0 resolutions increase from 30-250 m (30-60 min) before, to 15-200 m (15-30 min), after the EOLE system possible upgrade.

Based on actual bibliographical data the temperature profiles retrieved, currently, by Raymetrics lidar are provided with an accuracy better than 2K, and after upgrading the energy of the emitted laser power and implementing a second telescope, the accuracy is expected to be increased to better than 1K (range/time resolutions increase from 15 km/20 min to >20 km/1min). Moreover, the maximum range during daytime/nighttime could be increased from 4/17 to 8/>22 km after system's hardware upgrade.

5.5 Summary

The upgrading of the NTUA EOLE and Raymetrics lidar systems, although very limited by the available budget within the BIOSPHERE, is characterized adequate to meet the measurement requirements of the aerosol mass, atmospheric density, and temperature profiles, as discussed in Section 4.3.

6 Comparison of BIOSPHERE SCR detectors capabilities with each other and other neutron/muon detectors

The detection mechanisms for muons and neutrons differ due to their distinct properties. While muons, as charged particles, lose their energy via electromagnetic interactions (Bethe-Bloch mechanism), the detection of neutrons is more complex, as neutrons are charge-neutral. Neutrons are usually detected by reacting with absorbers or converters via a radiation capture, spallation, nuclear recoil, or similar reactions, producing charged particles which then generate a detectable signal. The choice of detector depends on the intended use and the criteria typically are such as the energy range, sensitivity, particle to be detected, detector dimensions, etc. Each type of detector has its advantages and limitations. Table 6.1 compares the capabilities of the detectors used in BIOSPHERE.

Table 6.1: Comparison of the detectors used in the BIOSPHERE project. The columns coloured grey indicate BIOSPHERE SCR detectors covered in sections 2, 3 and 4.

Detector	**UJF CAS neutron mobile detectors**	**ADVACAM Timepix stack telescope**	**SEVAN**	**3'' and 5'' spheres of Bonner Sphere Spectrometer (BSS)**	**DECOS2**	**DECOS1**
Sensitive material	EJ-309 liquid scintillator with 2.5% boron 10	Stack #1: 300 µm Si (top) + 1000 µm Si (bottom)[1] Stack #2: 500 µm Si (top) + 2000 µm CdTe (bottom)	plastic scintillator	He-3 gas proportional counter	EJ-200 plastic scintillator	EJ-200 plastic scintillator
Sensor dimensions (cm)	2''x2'': Ø 50.8 mm x 50.8 mm 5''x5'': Ø 127 mm x 127 mm	14.08 mm × 14.08 mm x thickness of given sensor	100 cm x 100 cm x 5 cm (4 slabs) and 50 cm x 50 cm x 25 cm (5 slabs)	Ø 76 mm Ø 127 mm	two units of 50 cm x 50 cm x 5 cm, each	two units of 80 cm x 80 cm x 2.5 cm, each
Sensor pixelization	No	Yes, 55 um pixel pitch	No	No	Yes, 5 cm pixel pitch	No
Whole detector dimensions	box with all components and both detectors - 66 x 49 x 24 cm3	11 cm x 3 cm x 2.5 cm	ca 120 cm x 120 cm x 280 cm	sphere of Ø 127 mm (full BSS set has spheres 3'' - 12'')	100 cm x 120 cm x 200 cm	173 cm x 99 cm x 143 cm

Detected particles **(Intended use)**	neutrons	Heavy charged particles (protons, ions), light charged particles (electrons, muons), photons (X rays, gamma rays[2]), neutrons (fast, thermal[3])	photons, neutrons, muons, charged particles	neutrons	muons	muons
Energy range	thermal to 10^1 MeV	neutrons: thermal neutrons, fast up to 100s MeV	up to 10^1 GeV	neutrons: thermal to 20 MeV (with spheres with Pb or W up to ~1 GeV)	1 MeV to 100 GeV	1 MeV to 100 GeV
Stray particle **(parasitic signal)**	photons	-	-	none	- electrons[6)] - high energy photons[7)]	- electrons - high energy photons
FOV	omnidirectional	thermal neutrons: 2pi (front side) fast neutrons, photons, charged particles: omnidirectional (4pi)	0.87 sr/2pi	omnidirectional	0.18 sr/2pi to 0.79 sr/2pi	0.79 sr/2pi
Spectrometric ability	Yes	Yes	No	No (yes only with full BSS set)	No	No
Time resolution (readouts per time interval)	individual events	individual events 100 ns time resolution	1 s (typically 1 min)	individual events	Individual events	10 min
Detection efficiency for thermal neutrons	2''x2'': 78.5 %	~1% (with ^{6}LiF converter)	-	3'': 2.3% 5'': 0.4%	-	-

	5''x5'': 84.8 %					
Detection efficiency for fast neutrons (Cf-252)	2''x2'': 25.3 % 5''x5'': 37.5 %	~0.2% (with polyethylene converter)[4] ~1% (with silicon sensor, direct channels)[5]	30% (at 200 MeV)	3'': 0.6% 5'': 1.4%	-	-

1) (Granja, 2022)
2) with limited detection efficiency, according photon energy
3) with limited detection efficiency, according converter mask and detection reaction channel (Granja, 2023)
4) (Oancea, 2023a)
5) (Granja, 2023)
6) Electron contribution can be reduced by increasing the separation between the two detector units.
7) Contributions from high-energy photons (for high natural background applications), including electrons and positrons, can be eliminated by using lead plate between the two detection units.

The comparison of DECOS2 with the PTB reference instrument is described in Section 2.4. While the reference instrument is less noisy, it lacks spatial resolution and has a fixed FOV. Other common portable detectors for muon detection are proportional counters (Wissmann, 2005), nuclear emulsion detectors (Lechmann, 2021) and novel semiconductor-based detectors (Granja, Kudela, Jakubek; 2018). While gas-based proportional counters have good sensitivity, they lack spatial resolution (they cannot be easily pixelated). Nuclear emulsion detectors have been used in a number of muon imaging experiments but are susceptible to strong background radiation from the environment and are passive. Semiconductor detectors, on the other hand, are superior in terms of both sensitivity and variability, but would be very expensive to cover a large active area.

The comparison of the novel UJF CAS neutron detector with SEVAN is described in Section 3.4. SEVAN is assembled from slabs of plastic scintillators - between two identical assemblies of 100 x 100 x 5 cm^3 scintillators are located two 100 x 100 x 5 cm^3 lead absorbers and thick 50 x 50 x 25 cm^3 scintillator assembly (Chilingarian et al., 2009; Chilingarian and Reymers 2008). A scintillator light capture cone and photomultiplier tube (PMT) are located on the top, bottom and the intermediate layers of the detector. Based on the combinations of the 3-layered detector output, the traversal particle can be identified. The absence of the signal in the upper scintillators, coinciding with the signal in the middle scintillator, points to neutral particle (neutron) detection. Sevan, like the neutron monitors used in environmental monitoring for detection of SCR, are large, heavy and stationary (not portable or movable). They can detect neutrons in a large energy range, but cannot discriminate between neutrons of various energies.

Bonner spheres spectrometer (BSS) is a spherical moderator system used for neutron spectrometry. The spectrometric method is based on the neutrons slowing down in moderator shells of different thickness and the thermal neutron counting by the detector placed in the centre of the moderator shell. The detector response depends on the moderator thickness and also on the incident neutron energy. The response functions are computed for each moderator thickness, forming the response matrix, characteristic for the typical thickness of the polyethylene shells (Roth, 2015). At CMI the BSS is composed of a set of polyethylene spheres with a diameter ranging from 3'' (7.62 cm) to 12'' (30.48 cm). The common useful upper energy range of such a spectrometer was extended with two additional spheres with added lead and tungsten layer. In the centre of each sphere there is a proportional counter with He-3 gas sensitive to thermal neutrons.

Semiconductor detectors (like Timepix) can be used as a neutron detector using a proper conversion layer. The detector efficiency for thermal and fast neutrons for the developed Timepix stack detectors is described in section 4.9.1.2.

7 References

Ansmann, A., et al., J. Geophys. Res.-Atmos., 116, D20, https://doi.org/10.1029/2010JD015567, 2011.

Baars, H., et al., Atmos. Chem. Phys., 19, 15183–15198, https://doi.org/10.5194/acp-19-15183-2019, 2019.

Chilingarian A., G. Hovsepyan, K. Arakelyan, S. Chilingaryan, V. Danielyan, K. Avakyan, A. Yeghikyan, A. Reymers, S. Tserunyan (2009) Space Environmental Viewing and Analysis Network (SEVAN), Earth Moon Planet 104, 195–210; DOI 10.1007/s11038-008-9288-1

Chilingarian A. and A. Reymers (2008) Investigations of the response of hybrid particle detectors for the Space Environmental Viewing and Analysis Network (SEVAN), Ann. Geophys., 26, 249–257.

Cooney, J.A., J. Appl. Meteor., 11, 108-112, 1972.

D'Amico, G., et al., Atmos. Meas. Tech., 8, 4891–4916, https://doi.org/10.5194/amt-8-4891-2015, 2015a.

D'Amico, G., Atmos. Meas. Tech. Discuss., 8, 10387–10428, doi:10.5194/amtd-8-10387-2015, 2015b.

De Rosa, B., et al., Atmos. Meas. Tech., 13, 405–427, 2020, https://doi.org/10.5194/amt-13-405-2020

Dombrowski H. and S Neumaier, Long-term PTB intercomparison of passive H*(10) dosemeters used in area monitoring 2012 JINST 7 P04017.

Enqvist, Andreas, et al. "Neutron light output response and resolution functions in EJ-309 liquid scintillation detectors." Nuclear Instruments and Methods in Physics Research Section A: Accelerators, Spectrometers, Detectors and Associated Equipment 715 (2013): 79-86

Granja,C., K. Kudela, J. Jakubek, et al, Directional detection of charged particles and cosmic rays with the miniaturized radiation camera MiniPIX Timepix, Nuclear Instruments and Methods in Physics Research Section A: Accelerators, Spectrometers, Detectors and Associated Equipment, Volume 911, 2018, pp. 142-152, https://doi.org/10.1016/j.nima.2018.09.140.

Granja, C., Jakubek, J., Polansky, S., Zach, V., Krist, P., Chvatil, D., et al. (2018). Resolving power of pixel detector Timepix for wide-range electron, proton and ion detection. Nucl. Instrum. Meth. A NIM-A, 908, 60–71. https://doi.org/10.1016/J.NIMA.2018.08.014

Granja C., Jakubek J., et. al, Spectral tracking of energetic charged particles in wide field-of-view with miniaturised telescope MiniPIX Timepix3 1×2 Stack, J. of Instrum. JINST 17 (2022) C03028, https://doi.org/10.1088/1748-0221/17/03/C03028

Granja C, Uhlar R, et al., Detection of fast neutrons with the pixel detector Timepix3, J. of Instrumentation JINST 18 (2023) P01003, https://doi.org/10.1088/1748-0221/18/01/P01003

Grieder, P. K. F., Cosmic Rays at Earth (Elsevier, 2001)

Groom, D.E., Mokhov, N.V., Striganov, S.I., 2001. Muon stopping power and range tables 10 MeV–100 TeV. At. Data Nucl. Data Tables 78, 183–356. https://doi.org/10.1006/adnd.2001.0861.

Haarig, M., et al., Atmos. Chem. Phys., 22, 355–369, https://doi.org/10.5194/acp-22-355-2022, 2022.

Klett, J.D., Appl. Opt. 20, 211. https://doi.org/10.1364/ao.20.000211, 1981.

Klett, J.D., Appl. Opt. 24, 1638. https://doi.org/10.1364/ao.24.001638, 1985.

Kokkalis, P., Atmosphere, 12(3), 1–26. https://doi.org/10.3390/atmos12030318, 2021.

Lechmann A., et al., Muon tomography in geoscientific research – A guide to best practice, Earth-Science Reviews 222 (2021) 103842.

Mattis, I., Atmos. Meas. Tech., 9, 3009–3029, https://doi.org/10.5194/amt-9-3009-2016, 2016.

Oancea, C., Granja, C., Marek, L., Jakubek, J., Šolc, J., Bodenstein, E., et al (2023). Out-of-field measurements and simulations of a proton pencil beam in a wide range of dose rates using a Timepix3 detector: Dose rate, flux and LET. Physica Medica, 106, 102529. https://doi.org/10.1016/J.EJMP.2023.102529

Oancea, C., Solc, J., Bourgouin, A., Granja, C., Jakubek, J., Pivec, J., Riemer, F., Vykydal, Z., Worm, S., & Marek, L. (2023a). Thermal neutron detection and track recognition method in reference and out-of-field radiotherapy FLASH electron fields using Timepix3 detectors. Physics in Medicine and Biology, 68(18), 185017. https://doi.org/10.1088/1361-6560/ACF2E1

Roth, C., Iorgulis, C., Visan, I., Cojocaru, G., Tencu, V., & Militaru, G. (2015). Bonner spheres neutron spectrometer development. In Turcu, Ilie (Ed.). Proceedings of NUCLEAR 2015 the 8th annual international conference on sustainable development through nuclear research and education Part 2/3, (p. 74). Romania: Institute for Nuclear Research - Pitesti.

Röttger A. and P. Kessler, Uncertainties and characteristic limits of counting and spectrometric dosimetry systems, Journal of Environmental Radioactivity 205–206 (2019) 48–54.

Sato, T. Analytical Model for Estimating Terrestrial Cosmic Ray Fluxes Nearly Anytime and Anywhere in the World: Extension of PARMA/EXPACS, PLOS ONE, 10(12): e0144679 (2015).

Sommer, M., Detection of Cosmic Radiation in the Atmosphere and Radiation Induced in Thunderclouds, PhD thesis, Czech Technical University in Prague, 2022.

Vykydal, Z., & Kralik, M. (2018). Characterisation of the graphite moderated thermal neutron field at CMI. Radiation Protection Dosimetry, 180(1–4), 51–55. https://doi.org/10.1093/RPD/NCX190

Weitkamp, C.: Lidar, Range-Resolved Optical Remote Sensing of the Atmosphere. Springer, 2005.

Werner, J.Ch., MCNP® User's Manual, Code Version 6.2, Los Alamos National Laboratory LA-UR-17-29981, 2017

Wissmann, F., V. Dangendorf, U. Schrewe, Radiation exposure at ground level by secondary cosmic radiation, Radiation Measurements 39 (2005) 95 – 104.

Zhang, ZX., Enqvist, T., Holma, M. et al. Muography and Its Potential Applications to Mining and Rock Engineering. Rock Mech Rock Eng 53, 4893–4907 (2020). https://doi.org/10.1007/s00603-020-02199-9